

SPECIES II. Stellar parameters of the EXPRESS program giant star sample

M. G. Soto¹, M. I. Jones², and J. S. Jenkins³

¹ School of Physics and Astronomy, Queen Mary University London, 327 Mile End Road, London E1 4NS, UK
e-mail: m.soto@qmul.ac.uk

² European Southern Observatory, Alonso de Córdova 3107, Vitacura, Casilla 19001, Santiago, Chile

³ Departamento de Astronomía, Universidad de Chile, Camino El Observatorio 1515, Las Condes, Santiago, Chile

Received XX; accepted XX

ABSTRACT

Context. As part of the search for planets around evolved stars, we can understand planet populations around significantly higher-mass stars than the Sun on the main sequence. This population is difficult to study any other way, particularly with radial-velocities to measure planet masses and orbital mechanics, since the stars are too hot and rotate too fast to present the quantity of narrow stellar spectral lines necessary to measure velocities at the few m/s level.

Aims. Our goal is to estimate stellar parameters for all of the giant stars from the EXPRESS project, which aims to detect planets orbiting evolved stars, and study their occurrence rate as a function of stellar mass.

Methods. We analyse high resolution echelle spectra of these stars, and compute their atmospheric parameters by measuring the equivalent widths for a set of iron lines, using an updated method implemented during this work. Physical parameters, like mass and radius, are computed by interpolating through a grid of stellar evolutionary models, following a procedure that carefully takes into account the post-main sequence evolutionary phases. The atmospheric parameters, as well as photometric and parallax data, are used as constraints during the interpolation process. Probabilities of the star being in the red giant branch (RGB) or the horizontal branch (HB) are estimated from the derived distributions.

Results. We obtain atmospheric and physical stellar parameters for the whole EXPRESS sample, which comprises a total of 166 evolved stars. We find that 101 of them are most likely first ascending the RGB phase, while 65 of them have already reached the HB phase. The mean derived mass is $1.41 \pm 0.46 M_{\odot}$ and $1.87 \pm 0.53 M_{\odot}$ for RGB and HB stars, respectively.

To validate our method, we compared our derived physical parameters with interferometry and asteroseismology studies. In particular, when comparing to stellar radii derived from interferometric angular diameters we find: $\Delta R_{\text{inter}} = -0.11 R_{\odot}$, which corresponds to a 1.7% difference. Similarly, when comparing with asteroseismology we obtain the following results: $\Delta \log g = 0.07 \text{ dex}$ (2.4%), $\Delta R = -0.12 R_{\odot}$ (1.5%), $\Delta M = 0.08 M_{\odot}$ (6.2%) and $\Delta \text{age} = -0.55 \text{ Gyr}$ (11.9%). Additionally, we compared our derived atmospheric parameters with previous spectroscopic studies. We find the following results: $\Delta T_{\text{eff}} = 22 \text{ K}$ (0.5%), $\Delta \log g = -0.03$ (1.0 %) and $\Delta [\text{Fe}/\text{H}] = -0.04 \text{ dex}$ (2%). We also find a mean systematic difference in the mass with respect to those presented in the EXPRESS original catalogue of $\Delta M = -0.28 \pm 0.27 M_{\odot}$, corresponding to a systematic mean difference of 16%. For the rest of the atmospheric and physical parameters we find good agreement between the original catalogue and the results presented here. Finally, we find excellent agreement between the spectroscopic and photometric $\log g$ values, showing the internal consistency and robustness of our method.

Conclusions. We show that our method, which includes a re-selection of iron lines and changes in the interpolation of evolutionary models, as well as higher quality GAIA parallaxes and newer extinction maps, can greatly improve the estimates of the stellar parameters for giant stars compared to what was presented previously. This method also results in smaller mass estimates, an issue that has been found in results for giant stars from spectroscopy in the literature. The results provided here will improve the physical parameter estimates of planetary companions found orbiting these stars, and give us insights into their formation and the effect of stellar evolution on their survival.

Key words. stars: fundamental parameters – stars: horizontal-branch – techniques: spectroscopic

1. Introduction

During the past 25 years, more than 4200¹ planets orbiting stars outside of our Solar System have been found, changing our views regarding planet formation and evolution. Thanks to numerous efforts to characterise the stars where these systems were found (and where no planet has been discovered yet), some correlations have come to light. One of them is the so-called planet-metallicity relation, in which there appears to be a positive correlation between giant planet fraction and stellar metallicity (Fis-

cher & Valenti 2005; Jenkins et al. 2017), and points to the core accretion model for planet formation as the most probable responsible mechanism (Ida & Lin 2004). The planet-metallicity relation has been well established for main-sequence stars with stellar masses $M < 1.5 M_{\odot}$, but it is still uncertain for more massive stars, with mixed results coming from different studies (Hekker & Meléndez 2007; Jones et al. 2016; Maldonado et al. 2013; Pasquini et al. 2007; Reffert et al. 2015). One reason for this is that intermediate-mass stars ($M > 1.5 M_{\odot}$), due to their high temperatures during the main sequence ($T_{\text{eff}} \gtrsim 6000 \text{ K}$), and their high rotational velocities ($\sim 140 \text{ km s}^{-1}$ for a $M \sim 1.5 M_{\odot}$ star; Royer et al. 2007), have fewer and broader absorption lines

¹ <http://exoplanet.eu>

than cooler objects, making them unfavourable candidates in radial velocity (RV) surveys as the measurement of radial velocities is more challenging (Borgniet et al. 2019; Galland et al. 2005; Lagrange et al. 2009). One way to access intermediate-mass stars for planet detection is to study them as they evolve off the main sequence. As a star evolves off the main sequence, its temperature decreases (more absorption lines in its spectra), as well as its rotational velocity (Schrijver & Pols 1993), resulting in narrower line profiles. These two effects translate into more precise RV measurements, allowing m/s RV precision to be achieved. As a result, during the last 20 years, multiple RV surveys have focused on evolved stars (Frink et al. 2001; Hatzes et al. 2005; Johnson et al. 2007; Jones et al. 2011; Niedzielski et al. 2007; Sato et al. 2005a; Setiawan et al. 2003; Wittenmyer et al. 2011).

The precise determination of the stellar parameters have direct repercussions in planetary studies, and therefore large programs generally set out to calculate the stellar parameters early in the program (e.g. Jenkins et al. 2008; Santos et al. 2003; Valenti & Fischer 2005). The physical characteristics (mass and radius) of a planet depend on the characteristics of the host star, and uncertainties in these values can be translated into uncertainties in planetary density and composition. The physical parameters for a main sequence star (like its mass) can be estimated from their position in the HR diagram (or colour-magnitude diagram), as evolutionary tracks for different masses are well separated from each other (for a given metallicity). That is not the case for evolved stars. Evolutionary tracks after the main sequence are degenerate in these diagrams, which means that stars with different masses and evolutionary states occupy very similar positions, making the solutions completely different depending on the chosen evolutionary state. This can be illustrated in Figure 1, where it can be seen that the Red Giant Branch (RGB) for a $2 M_{\odot}$ star lies very close to the Horizontal Branch (HB, sometimes also referred to as the Red Clump) of a $1 M_{\odot}$ star. For a given position in the HR diagram, the RGB solution will be more massive than the HB one. This can lead, for example, to the overestimation of the mass of a star's sample if the stars have been incorrectly assigned to the RGB (Stock et al. 2018; Takeda & Tajitsu 2015). If we correctly determine the star's evolutionary state, we can then estimate its position in the main sequence and then reconstruct the changes it went through up to the current state (Villaver et al. 2014).

The EXoPlanets aRound Evolved StarS (EXPRESS, Jones et al. 2011, hereafter J11) program studies a sample of 166 evolved stars in the southern hemisphere, looking for planetary companions using the radial velocity method. The program has already detected 19 planetary companions orbiting 17 giants stars (Jones et al. 2017, 2014, 2016, 2013, 2015a,b, 2020). Some targets in the sample also have companions detected by using combined datasets and also by other groups targeting common targets (Fischer et al. 2009; Johnson et al. 2011; Sato et al. 2012; Trifonov et al. 2014; Wittenmyer et al. 2016a,b, 2017). The aim of EXPRESS is to establish the rate of close-in planets ($P \leq 150$ days) around RGB and HB stars. There is observational evidence of a lack of close-in planets around evolved stars (Döllinger et al. 2009; Johnson et al. 2007; Jones et al. 2014, 2020; Sato et al. 2005b). Different possible scenarios have been proposed to explain this: tidal interaction between the star and planet after the star leaves the main-sequence, resulting in planetary engulfment (Kunitomo et al. 2011; Villaver & Livio 2009; Villaver et al. 2014), an inherent low gas giant formation efficiency at short orbital separations around intermediate-mass stars (Currie 2009),

and a rapid disk dissipation that prevents gas giants from migrating to close-in orbits (Ribas et al. 2015).

There has been ongoing debate over whether the mass of "massive" evolved planetary-host stars has been overestimated in the literature, and whether these stars are actually the evolved counterparts of F-G stars, as opposed to massive A-stars (Lloyd 2011, 2013; Schlafman & Winn 2013). In such a scenario, planet engulfment would likely result in a lack of close-in planets orbiting evolved stars, as we know of many close-in planets orbiting Sun-like stars on the main sequence (Schlafman & Winn 2013). This mass overestimation has also been found in studies of other datasets. For example, Stock et al. (2018) recomputed the masses of the targets from the Lick Planet Search (Frink et al. 2001) and compared them to those presented in Reffert et al. (2015). They found a ΔM_{\star} distribution with a mean value of $-0.12 M_{\odot}$ and standard deviation of $0.47 M_{\odot}$. The debate regarding the true mass distribution of giant stars in planet search surveys has continued (Ghezzi et al. 2018; Johnson et al. 2013; Sousa et al. 2015), and highlights the importance of comparing the mass estimates with results from other mass determination methods, for example, asteroseismology (Serenelli et al. 2020).

In this paper we discuss an extension of the SPECIES code (Soto & Jenkins 2018, hereafter SJ18), first used on main sequence stars, towards the giant phase. We present an update on the stellar parameters and evolutionary status for the EXPRESS sample, from what was presented in J11. We also compare our results with asteroseismic and interferometric studies, and find that they agree within the uncertainties. The paper is organised as follows: in Section 2 we present the EXPRESS stars sample; in Section 3 we describe the method used for the stellar parameters computation; in Section 4 we present and discuss our results, and how they compare to other works in the literature; finally, in Section 5 we present our conclusions and summary.

2. The sample

The EXPRESS program sample consists of 166² evolved stars, observable from the southern hemisphere ($\delta \leq +20$ deg). The stars were selected according to the following selection criteria: $0.8 \leq B-V \leq 1.2$, $-4.0 \leq M_V \leq 0.5$ and $V \leq 8.0$. These criteria allowed us to include relatively bright first-ascending red giant branch (RGB) stars, as well as clump giants, with intrinsic RV noise below $\sim 20 \text{ m s}^{-1}$ (Hekker et al. 2006; Sato et al. 2005a). In addition, we imposed a photometric variability ≤ 0.02 mag and parallax precision better than $\sim 14\%$, from the Hipparcos catalogue (Perryman et al. 1997). Finally, we excluded stars with known (sub)stellar companions from the sample.

As part of the EXPRESS project, we have collected multi-epoch high-resolution spectroscopic data for all 166 stars, using the Fiber-fed Extended Range Optical Spectrograph (FEROS; Kaufer et al. 1999), mounted on the MPG/ESO 2.2m telescope at La Silla Observatory, the decommissioned Fiber Echelle spectrograph (FECH) mounted on the 1.5m telescope at CTIO, and CHIRON (Tokovinin et al. 2013), which replaced FECH at the 1.5m telescope. Additional spectroscopic data were obtained using the Fiber Dual Echelle Optical Spectrograph (FIDEOS; Vanzi et al. 2018), at the 1 m UCN telescope at La Silla, to characterise binary companions (Bluhm et al. 2016) and we also retrieved HARPS archival data available for some of our targets.

The reduction of the FEROS and FIDEOS data was performed using the CERES pipeline (Brahm et al. 2017). Similarly, the CHIRON data were reduced with the Yale pipeline

² In the sample presented in J11 there were two missing stars.

(Tokovinin et al. 2013). In the case of HARPS, we used the ESO data reduction system.

3. Method

The data we used for the computation of the stellar parameters consist of the FEROS, CHIRON and HARPS spectra. In the case of FEROS data, we stacked together all the individual spectra to create a high signal-to-noise-ratio (SNR) template, which is also used to compute the RVs (see Jones et al. 2017), while for CHIRON and HARPS data, we simply used a high SNR observation. The spectra were analysed using SPECIES (SJ18), which relies on the equivalent width (EW) measurement of iron lines to estimate the atmospheric parameters (T_{eff} , $\log g$, $[\text{Fe}/\text{H}]$ and ξ_t , the microturbulence velocity). SPECIES uses MOOG (Snedden 1973), along with the equivalent widths and ATLAS9 model atmospheres (Castelli & Kurucz 2004) to solve the radiative transfer equation in local thermodynamical equilibrium (LTE) conditions. What follows is an iterative process in which the atmospheric parameters are modified until: 1) there is no correlation between the individual Fe I line abundances with the excitation potential and the reduced equivalent width (EW/λ); 2) the average abundance of Fe I and Fe II are the same, and 3) the obtained abundance of Fe I is the same as the one used to generate the model atmosphere of that iteration (Gray 2005).

The EWs were measured within SPECIES, by fitting Gaussian-shaped profiles to the absorption lines. The method is described in Section A. The linelist used is described in J11 and SJ18, with some modifications. We discarded the lines for which the EWs had large uncertainties ($\sigma_{\text{EW}}/\text{EW} \geq 0.5$) for most of the stars. We were finally left with 95 Fe I and 7 Fe II lines. Finally, for each individual spectrum, we only used lines with $10 \leq \text{EW} \leq 150 \text{ m\AA}$, to avoid very shallow lines that could be mistaken for noise in the continuum, and strong lines that no longer follow a Gaussian profile. The net affect of this selection is that we are biasing against lines formed very deep, or very high in the stellar photosphere.

The uncertainty in the atmospheric parameters derived by SPECIES is estimated from the uncertainty in the correlation between the iron abundance and the excitation potential (for the temperature), and between the abundance and the reduced EW (for the microturbulent velocity); for the metallicity, it is the spread of abundances from the Fe I lines, and for the surface gravity, it is derived from the spread of the Fe I and Fe II lines (details can be found in SJ18).

3.1. Initial parameters

Before starting the estimation of the atmospheric parameters, we gather photometric and astrometric information for each target. Parallax and proper motion were obtained from Gaia DR2 (Gaia Collaboration et al. 2018) or the Hipparcos mission (van Leeuwen 2007), 2MASS *JHK* magnitudes from Cutri et al. (2003), Tycho-2 (*BV*)_{*t*} magnitudes from Høg et al. (2000), Strömgren *b-y*, *m*₁, and *c*₁ from Hauck & Mermilliod (1998) or Holmberg et al. (2009), and Johnson *BV(RI)*_{*c*} magnitudes from Koen et al. (2010), Casagrande et al. (2006), Beers et al. (2007), or Ducati (2002). We also correct the magnitudes for dust extinction using the maps mentioned in Bovy et al. (2016), through the `mw dust`³ python package. For the case of the Gaia *G* magnitude, which is not included within the bandpasses of `mw dust`, we used $A_G = 2.35 E(B - V)$, from Bovy et al. (2014, 2016).

Table 1. Correspondance between Equivalent Evolutionary Points (EEPs) and stellar evolutionary phase.

EEP	Phase	Abbreviation
1	pre-main sequence	PMS
202	zero age main sequence	ZAMS
353	Intermediate age main sequence	IAMS
454	terminal age main sequence	TAMS
605	tip of the red giant branch	RGBTip
631	zero age core helium burning	ZACHeB
707	terminal age core helium burning	TACHeB

We preferred to compute our own extinction rather than using the A_G values provided in Gaia DR2 because we find that these are overestimated for the stars in our sample (average value of ~ 0.2 , when available), which are all nearby stars (average parallax $\sim 11 \text{ mas}$), away from the galactic centre, and therefore should experience low dust extinction in average. Finally, if the parallaxes were obtained from Gaia DR2, we apply the systematic correction from Stassun & Torres (2018)⁴.

We use the parallax, along with the proper motion, to estimate the evolutionary state of each target following the classification scheme presented in Collier Cameron et al. (2007). If the star is classified as a giant, we estimate its temperature following the relations from Alonso et al. (1999). In Section 4 we show how efficient that classification scheme was with our sample, and how the initial temperatures compare to the final values obtained from SPECIES.

Surface gravity was inferred as the minimum value between 3.5 and Equation 1 from SJ18. Finally, for all the stars in the giant sample, the metallicity was set to an initial value of zero.

3.2. Physical parameters

The physical parameters, namely mass, radius, age, luminosity, and evolutionary stage, were estimated using the latest version of the `isochrones`⁵ package (Morton 2015). This package creates a model of the star based on the atmospheric parameters, and estimates its physical parameters by interpolating through a grid of MESA Isochrones and Stellar Tracks (MIST, Dotter 2016) using MultiNest (Buchner et al. 2014; Feroz et al. 2009). The final values for each parameter will be drawn from the obtained distributions. The newest version of this package incorporates the interpolation of the isochrone grids using the equivalent evolutionary points (EEPs), which indicates the evolutionary stage of the star.

As described in Dotter (2016), EEPs are points in stellar evolution that can be identified in different evolutionary tracks, and are created to allow for the interpolation between tracks defined for different initial stellar masses. In the case of the MIST models, they are divided into primary EEPs, defined following a physical motivation, and secondary EEPs, that provide a uniform spacing between the primary EEPs. The phases that are relevant for this work are:

- Terminal Age Main Sequence (TAMS), defined as the point where the central H mass fraction is 10^{-2} , after which the

⁴ Recently, Chan & Bovy (2020) computed an updated zero-point parallax correction, but the value is within the uncertainties of the parallaxes for the stars in this study, therefore we decided to keep the correction from Stassun & Torres (2018) as it would not greatly affect our results.

⁵ <https://github.com/timothydmorton/isochrones>

³ <https://github.com/jobovy/mwdust>

star begins the burning of H outside the core and enters the RGB phase.

- Tip of the Red Giant Branch (RGBTip), the point at which the stellar luminosity reaches a maximum (or T_{eff} reaches a minimum), but before sustained He burning in the core has started. For low-mass stars ($M < 2.00 M_{\odot}$, Paxton et al. 2010), this point denotes the beginning of the helium flash, when He burning begins under degenerate conditions in the core.
- Zero Age Core Helium Burning (ZACHeB), where sustained core He burning begins, which will be referred to as the HB phase.
- Terminal Age Core Helium Burning (TACHeB), when the central He fraction is 10^{-4} , which denotes the end of the core helium burning. Subsequent evolutionary stages include the burning of He outside the core, and carbon burning for high-mass stars.

A more detailed description and processes involved in defining the EEPs can be found in Dotter (2016). The use of EEPs in isochrones allows for the correct interpolation in the isochrone grids for the evolved stellar phases⁶. As Dotter (2016) pointed out, inaccuracy in the interpolation happens because of the wide scale of changes the star goes through after the main sequence, all at very short timescales, compared to the time spent in the main sequence. During the post-main sequence phases, tracks for very similar initial masses will lie very close to each other but, for a certain age, will show stars in completely different evolutionary stages. A simple interpolation scheme that does not take into account the faster evolutionary phase after the MS might not be able to fully reproduce the morphology of the evolution track. This is one of the reasons for the discrepancy between the results presented here and those in J11. The numbers referred as EEPs in the rest of the text correspond to the secondary EEPs.

During the interpolation process, we adopted a prior mass distribution following a Salpeter initial mass function (IMF), with $\alpha = 2.35$. Similarly, we adopted a prior metallicity distribution, based on the local disk, following Casagrande et al. (2011)⁷. For the stellar age we adopted a flat prior in logarithmic scale, with bounds given as $(10^5 - 10^{10.15})$ yrs. Finally, the EEP has an uniform probability distribution, with 353 as the lower bound for giant stars (otherwise 200, to ensure no pre-main sequence stages), and 1710 as the upper bound. The atmospheric parameters derived previously (T_{eff} , $\log g$, and $[\text{Fe}/\text{H}]$), along with the photometric magnitudes and parallax (Section 3.1), were added to the likelihood function as $\ln L \propto -\frac{1}{2} \sum_i (x_i - I_i)^2 / \sigma_i^2$, where (x_i, σ_i) correspond to the observed and computed properties, and I_i is the model prediction for the i 'th parameter (Montet et al. 2015).

One of the outputs from the physical parameter estimation is the EEP distribution for each star. Table 1 shows the correspondence between EEP and evolutionary phase. For the rest of the analysis in the paper, we consider $454 < \text{EEP} < 631$ to be the RGB phase, and $631 \leq \text{EEP} \leq 707$ to be the HB phase. We also infer the probability of a star to be either in the RGB or the HB phase as $p_{\text{state}} = \sum \text{EEP}_{\text{state}} / \sum N$, where N is the total EEP distribution size distribution.

⁶ <https://isochrones.readthedocs.io/en/latest/modelgrids.html>

⁷ For a given metallicity value x , the probability density function takes the form $P(x) = w_0(w_1 N_1(x) + w_2 N_2(x))$, where $N_i = G(\mu_i, \sigma_i)$ represents a Gaussian distribution with parameters (μ_i, σ_i) , and the w_i terms are normalisation factors.

Table 2. Values obtained for the Sun spectra using SPECIES. Only average values are shown. Individual results for each spectrum are shown on Table B.5

Parameter	Unit	Value
Temperature	K	5770 ± 35
$[\text{Fe}/\text{H}]$	dex	-0.03 ± 0.04
$\log g$	cm s^{-2}	4.36 ± 0.04
ξ_t	km s^{-1}	0.82 ± 0.05
$v \sin i$	km s^{-1}	3.61 ± 0.19
v_{mac}	km s^{-1}	3.19 ± 0.15
Mass	M_{\odot}	0.97 ± 0.02
Radius	R_{\odot}	1.06 ± 0.05
Age	Gyr	6.9 ± 1.5
$\log L$	L_{\odot}	0.05 ± 0.06

3.3. Rotational and macroturbulent velocity

We followed the method described in SJ18 to compute the rotational and macroturbulent velocities, which we summarise here. The macroturbulent velocity is computed following equation 1 in dos Santos et al. (2016), and for the cases when we obtain a very small or negative value, indicating that the temperature and/or surface gravity is outside of the range of applicability, we adopt equation 2 from Brewer et al. (2016). The rotational velocity was estimated by fitting rotationally broaden synthetic profiles to five different absorption lines. To obtain an estimate of the uncertainty in the rotational velocities, we first vary the normalized flux of each line by an amount dy , with dy being drawn from a normal distribution with zero mean and width given by $1/\text{SNR}$, with SNR the signal-to-noise ratio of the spectrum. We then recompute the rotational velocity a total of 1000 iterations, obtaining a distribution of rotational velocities. The uncertainty is then taken as the standard deviation of the distribution. The final rotational velocity will correspond to the average of the velocities obtained for the five lines, with their corresponding errors. More details of the fitting procedure can be found in SJ18.

4. Results

The sample of giant stars from the EXPRESS project was first described and analysed in J11, using a broadly similar procedure to here for the estimation of atmospheric and physical parameters. Here we improve on this analysis by using updated versions of the atmospheric models and the MOOG code, unavailable when J11 was published. We also estimate the equivalent widths using the method described in section A, instead of using ARES (Sousa et al. 2007), as was done in J11. Additionally, here we use an updated version of the line list. We removed 68 lines from the original list used in J11, 54 Fe I and 14 Fe II lines, due to the consistently large uncertainties in the measured equivalent widths ($\sigma_{\text{EW}}/\text{EW} > 0.5$). The updated line list is given in Table B.1. In addition, here we used higher quality spectra to measure the EWs, in terms of resolving power and SNR. For ~ 30 stars presented in J11 we used FECH low SNR spectra at a resolution lower than FEROS and HARPS. As a consequence, the EWs and thus the derived atmospheric and physical parameters are largely uncertain. As an example we highlight the case of the planet-host star HIP 105854, for which we used a low quality FECH spectrum for the analysis. In J11 the obtained mass was $2.1 \pm 0.1 M_{\odot}$, a substantial overestimate of the mass obtained here ($0.97^{+0.09}_{-0.04} M_{\odot}$). This particular case was also noted by Campante et al. (2019), who used asteroseismology to derive a mass of $1.00 \pm 0.16 M_{\odot}$, if the star is in HB, as obtained here ($p_{\text{HB}} = 0.88$; see

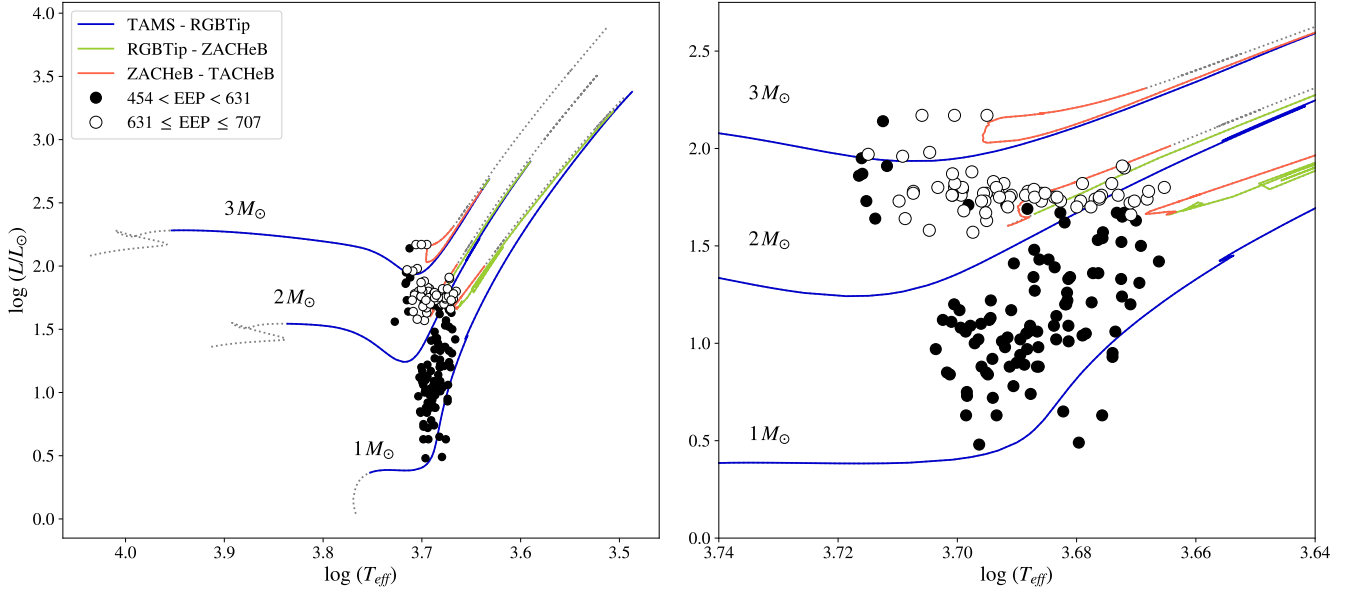


Fig. 1. H-R diagram of the giant star sample. The right panel is a close-up of the area where the stars in the sample are located. Open circles represent RGB stars, and filled circles HB stars. The tracks plotted have $[\text{Fe}/\text{H}] = 0.0$, and the different colours represent different phases in the stellar evolution. Grey lines represent the stages before the main sequence evolution (up to the TAMS, Table 1), and right after the end of core helium burning (TACHeB). For the meaning of the abbreviations and EEP number, see Table 1.

Table B.4). Finally, in the case of the physical parameters (like mass and radius), here we use the Gaia DR2 parallaxes, newer extinction maps and we also employ a different set of evolutionary models.

The HR diagram for the EXPRESS stars is shown in Figure 1. A sample of the catalogue produced by SPECIES, with a subset of columns, is shown in Table B.4. We also include in Table 2 the average values obtained for a set of Sun spectra, taken using different methods and instruments. The individual results are listed in Table B.5.

4.1. Comparison with the literature

We first analyse the stars from EXPRESS with results from interferometry and asteroseismology, which we use as a benchmark for the results obtained using our techniques. To this comparison we have also added a few other stars with spectra available from FEROS and HARPS, which are not necessary evolved stars. The list of stars with the results from SPECIES (for interferometry and asteroseismology) are listed in Table B.2, and the values from the literature in Table B.3. We then compare our results with other spectroscopic studies.

4.1.1. Interferometry

Precise stellar angular sizes can be obtained through long baseline interferometry, which can then be combined with parallax data and broadband photometry to estimate the size of a star. We compare a total of 12 targets (5 from the EXPRESS sample and 7 new targets with data from FEROS) with the radius from Gallenne et al. (2018), Tsantaki et al. (2013), and Rains et al. (2020), and the results are shown in Figure 2 and Table 3. In the case of Tsantaki et al. (2013), the authors do not explicitly list the radius found through interferometry, but show the limb-darkened an-

Table 3. Offsets between the radius from SPECIES, and from interferometry studies. μ , σ_μ , and σ are the mean, error in the mean, and standard deviation of the distribution from the residuals SPECIES-Literature, respectively.

Catalogues	Radius (R_\odot)			N
	μ	σ_μ	σ	
Gallenne et al. (2018)	-0.54	0.13	0.16	7
Rains et al. (2020)	-0.02	0.02	0.05	2
Tsantaki et al. (2013)	-0.00	0.01	0.03	4
Total ^a	-0.11	0.01	0.29	12

Notes. ^(a) The mean and error for the total values were computed using weights given by $w_i = (x_i/\sigma_i)^2$, with (x_i, σ_i) the value and uncertainty of each point i .

gular diameter θ_{LD} used. We combined θ_{LD} with parallax information from either Gaia or Hipparcos (whichever was the most precise) to obtain the stellar radius.

Overall, for interferometry we find a difference in the radius between SPECIES and the literature of $\Delta R_{\text{INTER}} = -0.11 \pm 0.29 R_\odot$, below the 2% level from the mean radius values. Here, the values are quoted as $\mu \pm \sigma$, the mean and standard deviation of the residual distribution, respectively. The comparison with interferometry is shown in Figure 2. We find that the differences in radius are within a standard deviation of the individual values (Table 3), where our results are $0.54 R_\odot$ ($\sim 5\%$) smaller Gallenne et al. (2018). These substantial differences are not seen when comparing with Tsantaki et al. (2013) and Rains et al. (2020), but those targets correspond to main sequence stars, whereas the targets from Gallenne et al. (2018) are giant stars.

Table 4. Offsets between the results from SPECIES, and from asteroseismic studies. μ , σ_μ , and σ are the mean, error in the mean, and standard deviation of the distribution from the residuals SPECIES-Literature, respectively.

Catalogues	logg (cgs)			Radius (R_\odot)			Mass (M_\odot)			Age (Age)			N
	μ	σ_μ	σ	μ	σ_μ	σ	μ	σ_μ	σ	μ	σ_μ	σ	
Morel et al. (2014)	0.13	0.05	0.09										5
Campante et al. (2019)	0.08	0.09	0.04	0.06	0.30	0.35	0.06	0.10	0.09	1.63	2.02	2.58	2
Jiang et al. (2020)	-0.04			-0.06			0.16			-2.86			1
Aguirre et al. (2020)	0.04	0.05	0.08	-0.08	0.25	0.27	0.04	0.08	0.14	-0.91	1.09	1.89	7
North et al. (2017)	-0.01	0.07	0.10	-0.06	0.15	0.14	0.01	0.12	0.10	-0.10	0.47	0.41	2
Total ^a	0.07	0.01	0.10	-0.12	0.01	0.26	0.08	0.03	0.12	-0.55	0.11	2.14	15

Notes. ^(a) The mean and error for the total values were computed using weights given by $w_i = (x_i/\sigma_i)^2$, with (x_i, σ_i) the value and uncertainty of each point i .

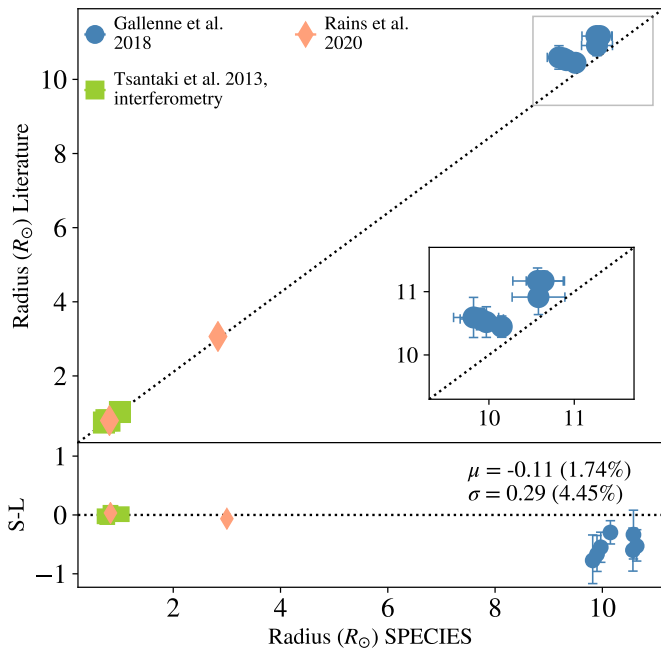


Fig. 2. Top panel: Comparison between the radius measurement from SPECIES and from works using interferometry, for the stars in our test sample. Black dotted line is the 1:1 relation. The inset correspond to a zoom of the squared regions. Bottom panel: Difference SPECIES-literature. Uncertainties are computed considering both SPECIES and literature values ($\sqrt{\sigma_{\text{SPECIES}}^2 + \sigma_{\text{Lit}}^2}$). The quoted text is the mean and standard deviation of the residuals, and their percentage from the mean radius value.

4.1.2. Asteroseismology

The asteroseismology technique consists of looking at stellar oscillation spectra from either spectroscopy or photometry, and measuring two global oscillation quantities: the average frequency separation ($\Delta\nu$), and the frequency corresponding to the maximum oscillation power (ν_{max}). In the case of solar-like oscillations, these values can then be used to estimate the stellar density and surface gravity by using scaling relations (Brown et al. 1991; Kjeldsen & Bedding 1995; Ulrich 1986), and by combining both quantities it is possible to obtain the stellar mass and radius, in a nearly model-independent approach. Another method widely used in the literature to obtain the stellar parameters is by using grid-based modelling techniques, that take as an input the individual frequency determinations or the global aster-

oseismic parameters, plus the effective temperature and metallicity, and other observational constraints. The scaling relations can also be included in the grid-based modelling. Even though this method is not model-independent, it has been found that the results given by the use of different pipelines, all using different stellar evolution models, are all in good agreement (Pinsonneault et al. 2018; Silva Aguirre et al. 2015). When the analysis is made using the grid-modelling approach, it is possible to also determine the stellar age. Age is a difficult parameter to fit for (Soderblom 2010), but asteroseismology has been so far the most precise method for its estimation, with uncertainties in the order of $\sim 25\%$ (Silva Aguirre & Serenelli 2016). The other properties derived from asteroseismology (like mass and radius) have been shown to be accurate to the $\sim 10\%$ level (Pinsonneault et al. 2018). A more detailed discussion on the subject of asteroseismology and the different pipelines available for the parameter estimation can be found in Chaplin & Miglio (2013); Silva Aguirre et al. (2020), and references therein.

We compared our estimates for the mass, radius, logg, and age for 15 targets (9 from EXPRESS, and 6 new targets with data taken with FEROS) with values computed using asteroseismology from Morel et al. (2014), Campante et al. (2019), Jiang et al. (2020), Aguirre et al. (2020), and North et al. (2017). In Morel et al. (2014), the surface gravity is computed from the scaling relation that uses ν_{max} and the stellar effective temperature. The temperature is computed from high-resolution spectroscopy, following the same method as in this work. As the authors do not list the values for $\Delta\nu$ and ν_{max} , it was not possible for us to separate the stellar mass and radius from the surface gravity. In Campante et al. (2019), Jiang et al. (2020), Aguirre et al. (2020), and North et al. (2017), the authors used temperature and metallicity values from the literature, and were used, together with the global asteroseismic parameters and astrometry information from Gaia (Hipparcos in the case of North et al. 2017), to retrieve the stellar parameters using grid-based modelling techniques. For Aguirre et al. (2020) and North et al. (2017), the logg values used for the comparison were estimated from their mass and radius results.

Figure 3 shows the comparison between SPECIES and the asteroseismic literature, and Table 4 lists the average differences. We find $\Delta \log g_{\text{ASTERO}} = 0.07 \pm 0.10$ dex, $\Delta R_{\text{ASTERO}} = -0.12 \pm 0.26 R_\odot$, $\Delta M_{\text{ASTERO}} = 0.08 \pm 0.12 M_\odot$, and $\Delta \text{Age}_{\text{ASTERO}} = -0.55 \pm 2.14$ Gyr. These offsets show agreement at the 2.4% level for the surface gravity, 1.5% for the radius, 6.2% for the mass, and 11.9% for the age. The standard deviations are within the 5% level for the surface gravity and the radius, within the 10% for the mass, and just within the 47% level for the age. We also

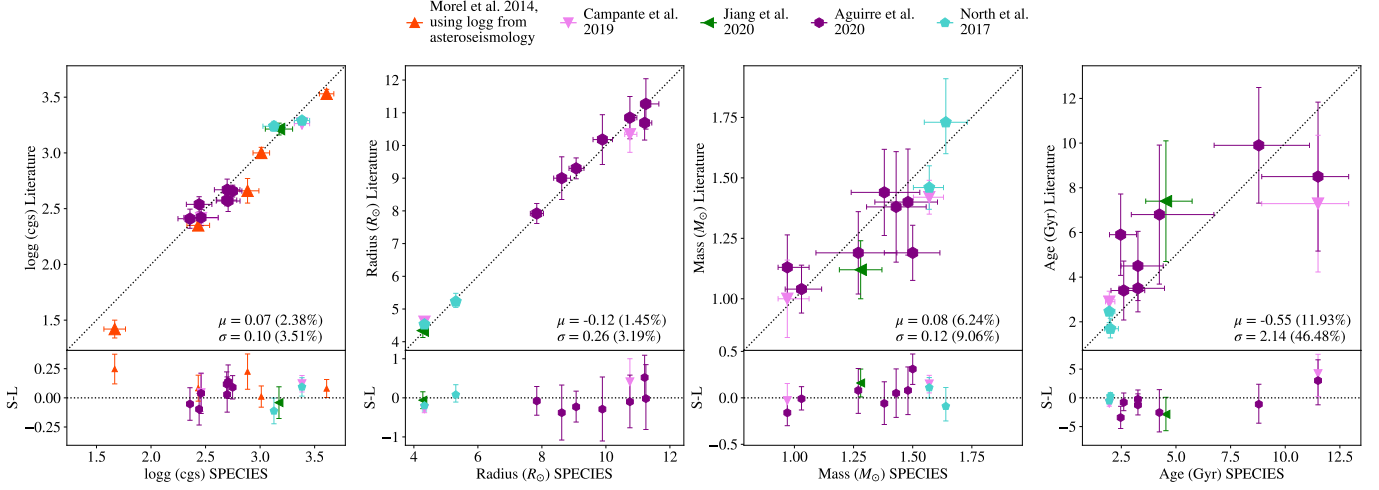


Fig. 3. Top panels: Comparison between SPECIES and the asteroseismology studies, for the stars in our test sample. Black dotted line in each panel is the 1:1 relation. Bottom panels: Difference SPECIES-literature, same as in Figure 2. The quoted text are the mean and standard deviation of the residuals for each quantity, and their percentage from the mean values. Surface gravity values were not given in Aguirre et al. (2020) and North et al. (2017), but were computed from their masses and radius.

highlight that the average offset with the radius agrees with the one from interferometry. For all the parameters, we are within a standard deviation of the residuals (SPECIES-Literature), which leads us to conclude that our results agree with the asteroseismology ones.

As we mentioned in the introduction, it is especially important to check the mass measurements of giant stars, computed using stellar evolution grids, with results from other methods. We find that our mass estimates, as a whole, agree with the asteroseismic values within the uncertainties (with the exception of HIP4293, from Aguirre et al. 2020). This result validates the mass estimates with SPECIES, which are shown for the whole EXPRESS sample in the next section.

4.1.3. Spectroscopy

We compared our results for the EXPRESS sample with works in the literature that use spectroscopy to derive the stellar parameters. These are Jones et al. (2011), Jofré et al. (2015), Luck & Heiter (2007), Alves et al. (2015), Wittenmyer et al. (2016), and the SWEET-Cat⁸ catalogue (Santos et al. 2013), a compilation of stellar parameters for stars with planets discovered in the literature. In the case of Luck & Heiter (2007), we compared with the parameters derived using spectroscopy, and from Alves et al. (2015), we used the results from the Tsantaki et al. (2013) line list, as those are the ones adopted by the authors. Figure 4 shows the comparison with our results and the mentioned works, for six of the parameters computed by SPECIES.

All these works from the literature use the same method for the derivation of the atmospheric parameters as in this paper, and differences arise in the source of the data (different instruments and S/N), the measurement of the equivalent widths, the model atmospheres, and the iron line list used. In the case of the physical parameters, when available, they were estimated using different stellar evolution models. The average differences, with their uncertainties, and dispersion in the residuals (SPECIES - Literature) are listed in Table 5.

For the temperature, we find that our results are in general larger than the literature ($\Delta T_{\text{spectro}} = 22 \pm 68$ K), but the dif-

ference is within a standard deviation of the data. In the case of the surface gravity and metallicity, our estimates are smaller than the literature, but both are within 1σ from zero, and represent less than 5% of the average $\log g$ and metallicity values for our sample. For the mass, our results are smaller than the literature ($\Delta M_{\text{spectro}} = -0.15 \pm 0.31 M_\odot$, which is mostly driven by the comparison with J11, which we would comment more on the next paragraph. The difference of $-0.25 M_\odot$ with respect to SWEET-Cat is driven mostly by four stars, two of which have large uncertainties ($\sigma \geq 0.45 M_\odot$), and if we remove those two objects the difference is reduced to $-0.11 M_\odot$. Finally, for both the radius and luminosity we find that our results agree with the literature values at the 2% level.

As we mentioned earlier, there has been some debate in the literature as to whether the masses of giant stars are overestimated when using stellar evolution codes, partly due to the challenge that poses interpolating through the post-main sequence tracks. This can be seen in our comparison with J11. We find an overall mass difference of $\Delta M_{\text{J11}} = -0.28 \pm 0.27 M_\odot$, with some targets being over $1 M_\odot$ smaller than in J11. This mass difference could be linked to what we already mentioned in the introduction: stellar evolution tracks are degenerate for giant stars. This means that tracks corresponding to different masses occupy the same region in the HR diagram. Although incorporating precise values for the temperature, surface gravity, and metallicity to the interpolation helps in achieving a more accurate mass determination (Sousa et al. 2015), this might not be enough. As we mentioned in section 3.2, the sampling of the evolution tracks in terms of the evolutionary state (the EEP in our case) helps in dealing with some of the complexity, as it takes into account, for example, how brief the post main sequence evolution is, compared to the total stellar lifetime (Dotter 2016; Girardi et al. 2013).

4.2. Comparison between $\log g$ and $\log g_{\text{iso}}$

Previous works have shown a systematic difference between the surface gravity derived from the ionization balance of iron lines (spectroscopic $\log g$), and from interpolation in a grid of evolutionary models, usually called photometric $\log g$ (e.g. Gratton

⁸ <https://www.astro.up.pt/resources/sweet-cat/>

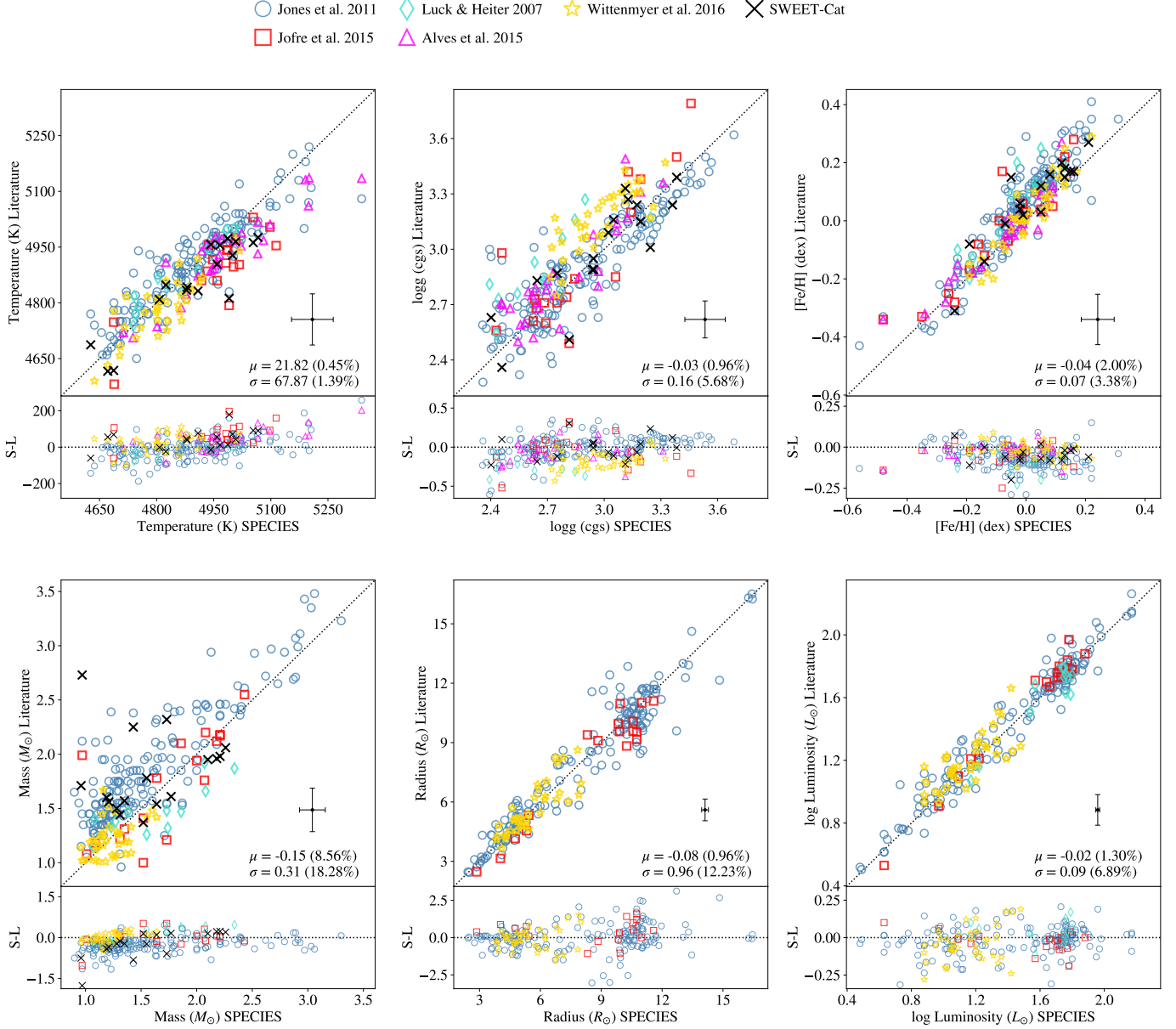


Fig. 4. Comparison between SPECIES and the literature for the EXPRESS stars. Bottom panels show the difference SPECIES-Literature. The errorbar shows the average uncertainties in the points. The quoted text are the mean and standard deviation of the residuals for each quantity, and their percentage from the mean values.

et al. 1996; Jofré et al. 2014; Jones et al. 2011; Sestito et al. 2006; Slumstrup et al. 2019; Tsantaki et al. 2019). Some of the proposed explanations for this disagreement are the line list used to compute the Fe II abundance, or problems with the fitting of the individual absorption lines, like line blending or incorrect placement of the continuum (Jones et al. 2011; Tsantaki et al. 2019), among others. Here, we also compared our derived spectroscopic and photometric $\log g$'s. Figure 5 shows our comparison between these two independent values. As can be seen we find a good agreement between them, with an average difference of only 0.001 dex, well below the individual mean $1-\sigma$ uncertainty. We find a few exceptions, for which $|\log g - \log g_{\text{iso}}| > 0.22$ dex. This value was derived in SJ18 after studying the difference in both quantities. For those stars, $\log g_{\text{iso}}$ was adopted and the stellar parameters were recomputed, following SJ18. We found that by imposing $\log g_{\text{iso}}$ as the final $\log g$ value, the rest of the pa-

rameters (T_{eff} , $[\text{Fe}/\text{H}]$, and the other physical parameters) were barely affected, with changes that are within their respective uncertainties.

4.3. Initial parameters effectiveness

As was mentioned in section 3.1, we used the scheme from Collier Cameron et al. (2007) to classify the stars processed with SPECIES as dwarf or giant stars. Figure 6 replicates Figure 8 from Collier Cameron et al. (2007), but with the EXPRESS sample. We find that, following this scheme, 93% of stars were correctly classified as giant.

The initial temperature was derived from photometric information for each star, using the relations from Alonso et al. (1999). Even though photometric relations are available for 12 colours within the paper, we only used the ones corresponding

Table 5. Residuals between our results and the literature. μ , σ_μ , and σ correspond to the mean, error in the mean, and standard deviation of the residual distribution, respectively. The last column shows the number of stars in common with each catalogue.

Catalogue ^a	Temperature (K)			logg (cgs)			[Fe/H] (dex)			M/M_\odot			R/R_\odot			log L/L_\odot			N
	μ	σ_μ	σ	μ	σ_μ	σ	μ	σ_μ	σ	μ	σ_μ	σ	μ	σ_μ	σ	μ	σ_μ	σ	
J11	-4.09	7.56	69.82	0.00	0.01	0.16	-0.06	0.01	0.07	-0.28	0.01	0.27	-0.02	0.02	1.03	-0.021	0.001	0.090	166
J15	67.70	14.77	60.58	-0.06	0.03	0.20	-0.05	0.02	0.07	-0.00	0.05	0.33	0.40	0.15	0.73	-0.026	0.025	0.068	17
L07 ^b	-13.32	14.83	33.03	-0.21	0.03	0.14	-0.10	0.03	0.06	0.14	0.05	0.26				0.035	0.004	0.075	12
A15 ^c	49.75	12.38	56.71	-0.07	0.03	0.12	-0.02	0.01	0.05										27
W16	27.10	9.54	47.84	-0.18	0.02	0.10	-0.02	0.01	0.05	0.01	0.02	0.18	-0.10	0.02	0.69	-0.044	0.002	0.113	37
SC ^d	43.47	20.25	53.23	-0.01	0.05	0.15	-0.05	0.02	0.06	-0.25	0.07	0.50							17
Total ^e	21.82	0.01	67.87	-0.03	0.01	0.16	-0.04	0.01	0.07	-0.15	0.01	0.31	-0.08	0.01	0.96	-0.018	0.001	0.093	

Notes. (a) J11: Jones et al. (2011), J15: Jofré et al. (2015), L07: Luck & Heiter (2007), A15: Alves et al. (2015), W16: Wittenmyer et al. (2016), SC: SWEET-Cat.

(b) The parameters used correspond to the spectroscopic ones, and the mass obtained using the spectroscopic T_{eff} .

(c) Only the results from using the line-list from Tsantaki et al. (2013).

(d) We only considered the data from their homogeneous sample, meaning that the parameters were derived following the uniform methodology described in Santos et al. (2013). The individual stars were analysed in Mortier et al. (2013), Andreasen et al. (2017), and Sousa et al. (2018).

(e) The mean and error for the total values were computed using weights given by $w_i = (x_i/\sigma_i)^2$, with (x_i, σ_i) the value and uncertainty of each point i .

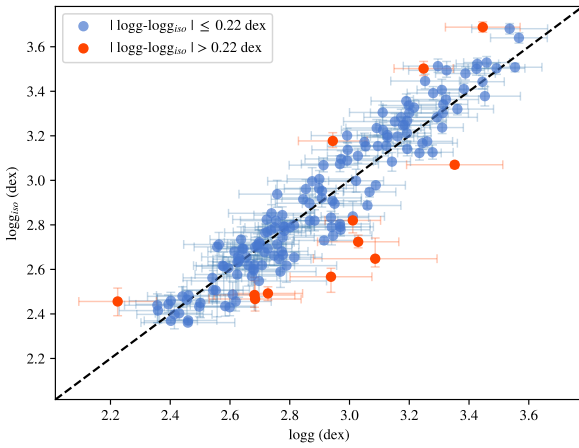


Fig. 5. Comparison between logg and logg_{iso}. The black dashed line represents the 1:1 relation.

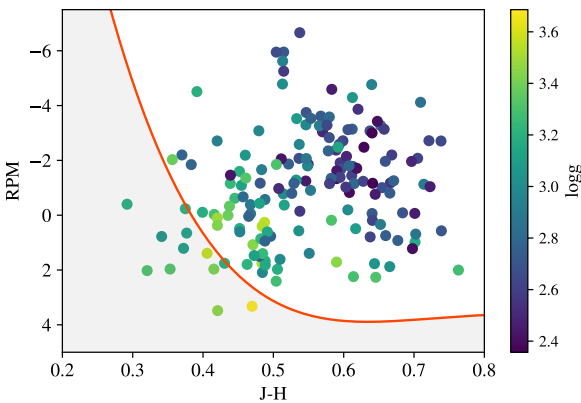


Fig. 6. Giant star classification, using the prescription from Collier Cameron et al. (2007). RPM (reduced proper motion) is defined as $J + 5 \log(\mu)$, with μ the proper motion. The red line is the boundary between the dwarf and giant stars region. Points falling in the grey area are classified as dwarf stars.

Table 6. Linear fit parameters between the temperature obtained using the colour relations from Alonso et al. (1999) and SPECIES, with $T_{\text{COLOUR}} - T_{\text{SPECIES}} = a T_{\text{COLOUR}} + b$.

Colour	a	b
V-K	0.759	3710
J-H	0.920	4525
J-K	0.769	3847

to $V-K$, $J-H$, and $J-K$. That is because we had very few stars with precise magnitude measurements in the remaining bands, and therefore we could not test the reliability of the temperature relations for those colours. As is shown in Alonso et al. (1999), the temperature relations also depend on the stellar metallicity. In the case of the initial parameters, we would have to use a photometric estimate of the metallicity. Most of the relations found in the literature use the Strömgren photometric system, but only a small number of stars in our sample had those magnitudes available. Therefore, we decided to set the initial metallicity to zero for all the stars in the sample.

The individual temperatures using the relations from Alonso et al. (1999), referred to as T_{colour} , for $[\text{Fe}/\text{H}] = 0$, compared to the final values from SPECIES, are shown in Figure 7. We find that in all three cases, it is possible to relate both values through a linear fit of the form

$$T_{\text{COLOUR}} - T_{\text{SPECIES}} = a T_{\text{COLOUR}} + b, \quad (1)$$

with a and b listed in Table 6. The final temperature from photometry, referred to as T_{photo} , is taken as the average weight of the individual colour temperatures, with the weights given by the uncertainty in the temperature estimates, computed from the uncertainties in the magnitude measurements, and the intrinsic uncertainties from the colour temperature relations, given in Alonso et al. (1999). In Figure 8, we show the histogram of the difference between the values from SPECIES with the final temperature average from photometry. In the case where no correction is applied to the individual colour relations, we find an offset of 358 K with respect to the SPECIES values, whereas if the correction is applied, that offset is reduced to 9 K.

We studied the effect of imposing $[\text{Fe}/\text{H}] = 0$ in the computation of T_{photo} by repeating the same analysis as before, but for two cases: setting $[\text{Fe}/\text{H}]$ equal to the mean value found by

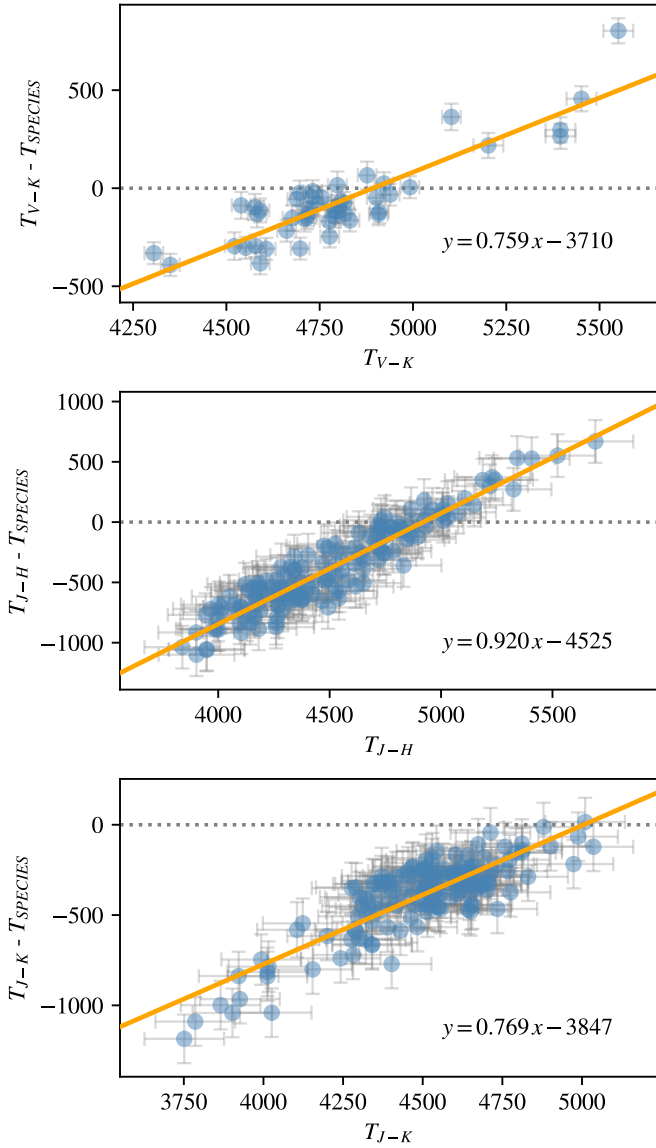


Fig. 7. Comparison between temperature computed with the photometric relations from [Alonso et al. \(1999\)](#), and SPECIES. Orange line represents the linear fit to the data, quoted in the text.

SPECIES for the whole sample, -0.03 dex (Table 7), and using the metallicity computed by SPECIES for each individual star. We find that the parameters a and b from equation 1 do not change considerably, and that the mean difference between $T_{\text{SPECIES}} - T_{\text{photo}}$ changes at most by 5 K compared to the values from setting $[\text{Fe}/\text{H}] = 0$. We conclude that, for the stars in this sample, the assumption of $[\text{Fe}/\text{H}]_{\text{ini}} = 0$ does not affect the value for T_{ini} from photometry.

4.4. Correlation between parameters

We studied the degree of correlation between the parameters derived by SPECIES. Figure 9 shows the most clear cases we detected (correlations for all the parameters are shown in Figure B.1). After fitting polynomial functions to the data, we derived equations 2-7.

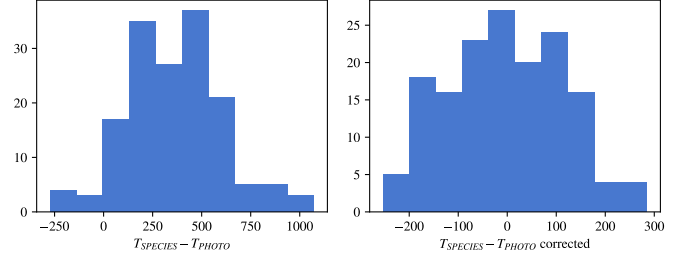


Fig. 8. Histogram of the difference between the temperature from SPECIES, and from photometry, before (left panel) and after correcting (right panel) by the linear fits.

$$\log g = (4.13 \pm 0.05) - (1.43 \pm 0.05) \log R \quad (2)$$

$$\xi_t = (2.95 \pm 0.09) - (0.57 \pm 0.03) \log g \quad (3)$$

$$\log(\text{Age}) = (9.97 \pm 0.01) - (3.00 \pm 0.02) \log M \quad (4)$$

$$\log L = -(0.28 \pm 0.01) + (1.97 \pm 0.01) \log R \quad (5)$$

$$\log v_{\text{mac}} = (0.23 \pm 0.01) + (0.34 \pm 0.01) \log R \quad (6)$$

$$v_{\text{mac}} = (0.86 \pm 0.16) + (0.67 \pm 0.04) v \sin i \quad (7)$$

The relation between the surface gravity and radius is expected by the physical definition of the surface gravity: $g = GM/R^2$, where G is the gravitational constant, which can be rewritten as $\log g \sim a(M) - b \log R$, with $a(M)$ a value that depends on the mass. The mass range covered by the EXPRESS sample is for the most part very narrow (78% of the stars have $0.85M_{\odot} \leq M \leq 2M_{\odot}$), which allows us to approximate $a(M)$ into a constant.

The relationship between microturbulence and surface gravity had been spotted before ([Adibekyan et al. 2015](#); [Jones et al. 2011](#); [Kirby et al. 2009](#); [Monaco et al. 2005](#); [Mucciarelli & Bonifacio 2020](#)), and takes the same shape as it does here ($\xi_t = a + b \log g$). The coefficients we found ($a = 2.95$, $b = -0.57$) agrees with the ones found in [Jones et al. \(2011\)](#).

The age-mass relation is related to the fact that, once a star reaches the red giant phase, its age can be determined by the amount of time it spent in the main sequence ([Casagrande et al. 2016](#)). The time in the main sequence is directly related to the mass of the star, following $t_{\text{MS}} \propto M^{-2.5}$. In our case, we find the power-law coefficient to be -3.0 .

The luminosity is directly related to radius by its definition: $L \propto R^2 T^4$. As the range of temperatures mapped by the stars of the EXPRESS sample is narrow ($\sigma_T = 128$ K), we can set the temperature dependence as a constant, which leads us to Equation 5.

Finally, we derive two equations that relate the macroturbulent velocity, the radius, and the rotational velocity. We see that the macroturbulent velocity saturates out at for the faster rotating stars, since the line profile is dominated by rotation in these cases, no matter the stellar spectral type. The macroturbulence is driven by the stellar convective flows, and hence temperature, whereas the rotation velocity is tied to the evolution, and hence given the range of temperatures we are sensitive to, we can expect the rotation velocity to span a much wider range than the macroturbulent velocity.

4.5. Evolutionary stage

As mentioned in Section 3.2, one of the outputs from isochrones is the EEP state for each star. We consider the final

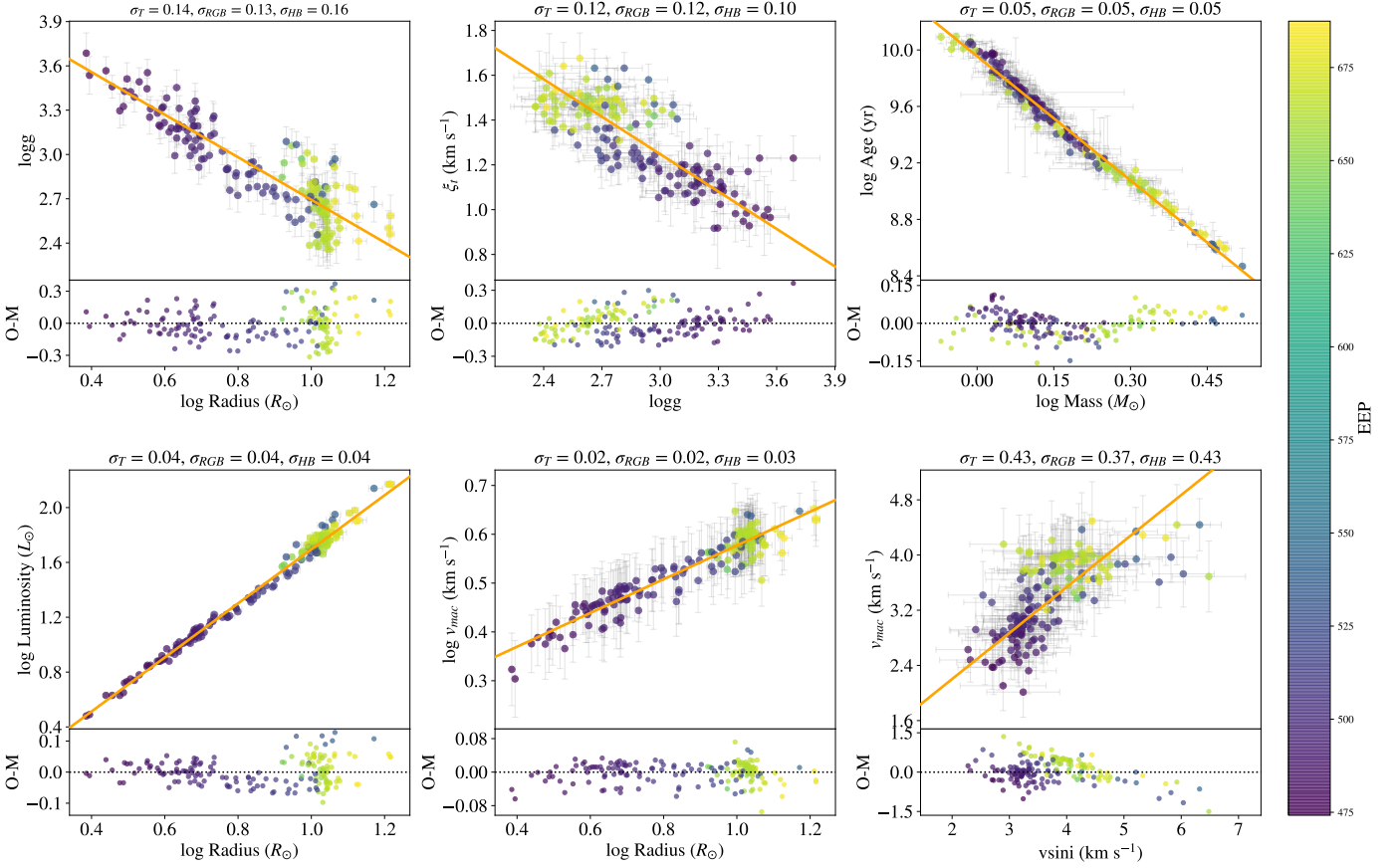


Fig. 9. Correlations found between parameters derived in this work. The orange lines are the polynomial fits. Bottom panels are the residuals after subtracting the polynomial fits. The colour scale represents the median EEP for each target. Titles show the scatter in the residuals for the total sample (σ_T), stars in the RGB (σ_{RGB}) and in the HB (σ_{HB}).

Table 7. Mean and standard deviation for the parameters derived with SPECIES, and how they change with evolutionary stage.

	Total	RGB	HB
Temperature (K)	4892 ± 138	4886 ± 138	4902 ± 139
[Fe/H] (dex)	-0.03 ± 0.14	-0.01 ± 0.13	-0.05 ± 0.14
$\log g$ (cgs)	2.89 ± 0.31	3.05 ± 0.28	2.65 ± 0.17
ξ_t (km s ⁻¹)	1.31 ± 0.19	1.21 ± 0.16	1.47 ± 0.07
Mass (M_\odot)	1.59 ± 0.54	1.41 ± 0.46	1.87 ± 0.53
Radius (R_\odot)	7.99 ± 3.29	6.00 ± 2.49	11.07 ± 1.53
$\log L$ (L_\odot)	1.42 ± 0.40	1.19 ± 0.34	1.79 ± 0.11
$\log \text{Age}$ (yr)	9.43 ± 0.39	9.57 ± 0.34	9.20 ± 0.35
$v \sin i$ (km s ⁻¹)	3.73 ± 0.76	3.48 ± 0.75	4.13 ± 0.60
v_{mac} (km s ⁻¹)	3.41 ± 0.55	3.11 ± 0.49	3.87 ± 0.24

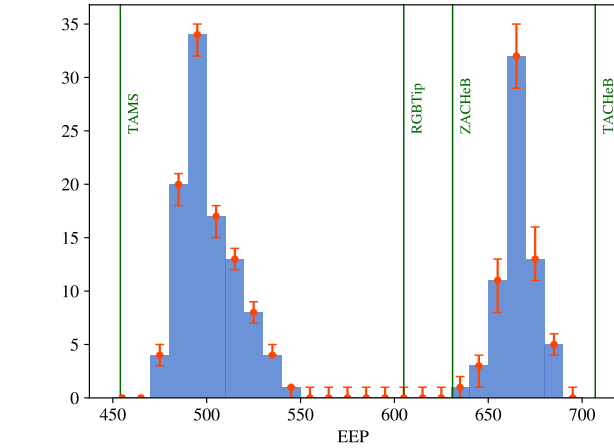


Fig. 10. Distribution of the stellar evolutionary stage of the star. The errors in each bin reflect the uncertainty in the EEP values, given by the 16% and 84% percentiles of the EEP distribution for each star.

EEP value for a certain star to be the median of the EEP distribution, and follow the RGB and HB definition from Section 3.2. Figure 10 shows the distribution of EEP values for our sample. We find that 61% of stars (101) are in the RGB phase, while the other 39% (65) are in the HB.

Figure 11 shows the distribution of the stellar parameters as a function of evolutionary stage, with mean values separated into total, RGB, and HB distribution listed in Table 7. We find that there is no difference in the temperature and metallicity distributions between RGB and HB stars. We also find that the EXPRESS sample is slightly metal poor ($[\text{Fe}/\text{H}] = -0.03$ dex), which is similar to what has been seen in other radial velocity searches around evolved stars (Döllinger et al. 2009; Mortier et al. 2013).

When looking at the size distribution, HB stars dominate the distribution for $R > 9 R_\odot$, and in turn have, on average, larger radii than RGB stars. They are also distributed around

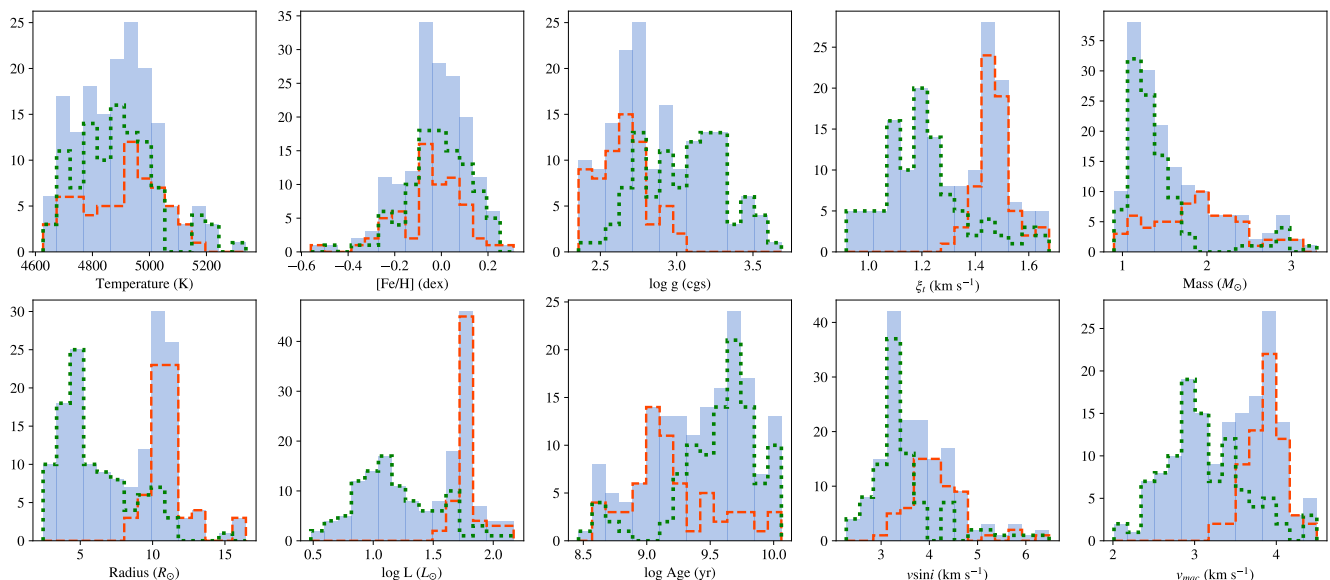


Fig. 11. Distribution of some of the parameters derived by SPECIES, separated by their evolutionary stage. The red line corresponds to the HB distribution, and the green line to the RGB distribution. The blue histogram represents the total of both distributions.

$8.3 < R/R_{\odot} < 16.5$, whereas RGB stars can cover a larger range, with $2.4 < R/R_{\odot} < 15$. This radius difference between RGB and HB stars is reflected in the distribution of luminosity, surface gravity, micro and macroturbulence velocity, because of the correlations found in Section 4.4. We find that HB stars are more luminous, have on average smaller $\log g$, and larger micro and macro turbulent velocity, than RGB stars.

Low-mass stars ($M < 2M_{\odot}$) are mostly found in the RGB phase (69%), which is explained by the fact that the evolutionary timescale of this phase is longer for these stars than more massive stars, and therefore is more probable to find them at that stage. The near lack of RGB stars with masses $M > 2M_{\odot}$ is explained by the fact that intermediate mass stars do not go through the helium-flash (the ignition of helium burning in the stellar core from degenerate conditions) and therefore the lifetime of the RGB phase is much shorter than for lower-mass stars (Girardi et al. 2013). HB stars also cover a large range of possible masses (from $0.9 M_{\odot}$ to $3.06 M_{\odot}$), but RGB stars are mostly clustered around $1.4 M_{\odot}$. The dispersion of the residuals from the correlations adjusted in the previous section are large for HB stars in the case of the radius with $\log g$. That could be explained by our approximation of the mass dependency on equation 2 to a constant, which is better fitted for RGB stars with a narrow range of masses, than for HB stars.

Finally, we find that HB stars have on average larger rotational velocities than RGB stars.

5. Summary and conclusions

In this work we present atmospheric and physical parameters of the EXPRESS program sample, derived using the SPECIES code. In this work we have introduced some improvements to SPECIES, including an updated version of the line list, a new routine to measure EWs of the iron lines and the addition of the EEP into the interpolation of evolutionary models. Similarly, here we use higher quality stellar templates, more accurate parallaxes from the Gaia DR2 and newer extinction maps, compared to the original catalogue. Based on the posterior probabilities, we find that 101 stars are most probably in the RGB, and 65 in

the HB. The separation of both stages is important not only for breaking the degeneracy in the H-R diagram and the correct estimation of the stellar mass, but also for the study of the effect of stellar evolution in planetary systems.

We compare our results with asteroseismology studies. Overall we find an agreement at the 2% level in the stellar radii and at the 6% level in the stellar mass. By comparing our stellar radii with interferometric studies we also find an agreement better than 2%. These results validate our method and show the robustness of SPECIES to accurately derived stellar parameters.

Similarly, we compared our temperature, surface gravity, metallicity, mass, radius, and stellar luminosity with estimates from other spectroscopic catalogues. We find good agreement for all the parameters, with mean differences within 2%. The only exception is the mass, for which we find an overall difference of $-0.15 M_{\odot}$, corresponding to $\sim 9\%$ difference. The largest differences are with respect to J11. This could be due to the differences in the line list, the stellar evolution models and interpolation procedure, the quality of the spectra used, or to the complexity of estimating stellar masses for giant stars using stellar evolution tracks, as these are degenerate in the parameter space giant stars occupy.

In addition, we studied the correlations between the parameters and find six relations, most of them driven by physical processes ($\log g$ -radius, age-mass, and luminosity-radius) and others already detected in previous works (microturbulence- $\log g$). We also detect relations between the macroturbulence velocity and the radius, and between the macroturbulence and rotational velocity.

Finally we compared our spectroscopic and photometric $\log g$'s, to investigate for any potential systematic difference, as has been widely reported in the literature. We find an excellent agreement between these two quantities, with a mean difference of 0.001 dex. Again this result shows the internal consistency and robustness of the method.

Acknowledgements. MGS acknowledges support from STFC through the Consolidated Grant ST/M001202/1. JSJ acknowledges support by FONDECYT grant 1201371 and partial support from CONICYT project Basal AFB-170002. This research has made use of the VizieR catalogue access tool, CDS, Strasbourg,

France (DOI : 10.26093/cds/vizieR). The original description of the VizieR service was published in 2000, A&AS 143, 23.

References

- Adibekyan, V. Z., Benamati, L., Santos, N. C., et al. 2015, MNRAS, 450, 1900
- Aguirre, V. S., Stello, D., Stokholm, A., et al. 2020, ApJ, 889, L34
- Alonso, A., Arribas, S., & Martínez-Roger, C. 1999, A&AS, 140, 261
- Alves, S., Benamati, L., Santos, N. C., et al. 2015, Monthly Notices of the Royal Astronomical Society, 448, 2749
- Andreasen, D. T., Sousa, S. G., Tsantaki, M., et al. 2017, A&A, 600, A69
- Aurière, M. 2003, in EAS Publications Series, Vol. 9, EAS Publications Series, ed. J. Arnaud & N. Meunier, 105
- Bedell, M., Bean, J. L., Meléndez, J., et al. 2017, ApJ, 839, 94
- Beers, T. C., Flynn, C., Rossi, S., et al. 2007, ApJS, 168, 128
- Blanco-Cuaresma, S., Soubiran, C., Jofré, P., & Heiter, U. 2014, A&A, 566, A98
- Bluhm, P., Jones, M. I., Vanzi, L., et al. 2016, A&A, 593, A133
- Boggs, P. T. & Rogers, J. E. 1990, Contemporary Mathematics, 112, 183
- Borgniet, S., Lagrange, A. M., Meunier, N., et al. 2019, A&A, 621, A87
- Bovy, J., Nidever, D. L., Rix, H.-W., et al. 2014, ApJ, 790, 127
- Bovy, J., Rix, H.-W., Green, G. M., Schlafly, E. F., & Finkbeiner, D. P. 2016, ApJ, 818, 130
- Brahm, R., Jordán, A., & Espinoza, N. 2017, PASP, 129, 034002
- Brewer, J. M., Fischer, D. A., Valenti, J. A., & Piskunov, N. 2016, ApJS, 225, 32
- Brown, T. M., Gilliland, R. L., Noyes, R. W., & Ramsey, L. W. 1991, ApJ, 368, 599
- Buchner, J., Georgakakis, A., Nandra, K., et al. 2014, A&A, 564, A125
- Campante, T. L., Corsaro, E., Lund, M. N., et al. 2019, ApJ, 885, 31
- Casagrande, L., Portinari, L., & Flynn, C. 2006, MNRAS, 373, 13
- Casagrande, L., Schönrich, R., Asplund, M., et al. 2011, A&A, 530, A138
- Casagrande, L., Silva Aguirre, V., Schlesinger, K. J., et al. 2016, MNRAS, 455, 987
- Castelli, F. & Kurucz, R. L. 2004, ArXiv Astrophysics e-prints [astro-ph/0405087]
- Chan, V. C. & Bovy, J. 2020, MNRAS, 493, 4367
- Chaplin, W. J. & Miglio, A. 2013, Annual Review of Astronomy and Astrophysics, 51, 353
- Collier Cameron, A., Wilson, D. M., West, R. G., et al. 2007, MNRAS, 380, 1230
- Currie, T. 2009, The Astrophysical Journal, 694, L171
- Cutri, R. M., Skrutskie, M. F., van Dyk, S., et al. 2003, 2MASS All Sky Catalog of point sources.
- Dekker, H., D’Odorico, S., Kaufer, A., Delabre, B., & Kotzlowski, H. 2000, in Society of Photo-Optical Instrumentation Engineers (SPIE) Conference Series, Vol. 4008, Proc. SPIE, ed. M. Iye & A. F. Moorwood, 534–545
- Döllinger, M. P., Hatzes, A. P., Pasquini, L., Guenther, E. W., & Hartmann, M. 2009, A&A, 505, 1311
- dos Santos, L. A., Meléndez, J., do Nascimento, J.-D., et al. 2016, A&A, 592, A156
- Dotter, A. 2016, ApJS, 222, 8
- Ducati, J. R. 2002, VizieR Online Data Catalog
- Feroz, F., Hobson, M. P., & Bridges, M. 2009, MNRAS, 398, 1601
- Fischer, D., Driscoll, P., Isaacson, H., et al. 2009, ApJ, 703, 1545
- Fischer, D. A. & Valenti, J. 2005, The Astrophysical Journal, 622, 1102
- Frink, S., Quirrenbach, A., Fischer, D., Röser, S., & Schilbach, E. 2001, PASP, 113, 173
- Gaia Collaboration, Brown, A. G. A., Vallenari, A., et al. 2018, A&A, 616, A1
- Galland, F., Lagrange, A. M., Udry, S., et al. 2005, A&A, 443, 337
- Gallenne, A., Pietrzyński, G., Graczyk, D., et al. 2018, A&A, 616, A68
- Ghezzi, L., Montet, B. T., & Johnson, J. A. 2018, ApJ, 860, 109
- Girardi, L., Marigo, P., Bressan, A., & Rosenfield, P. 2013, The Astrophysical Journal, 777, 142
- Gratton, R. G., Carretta, E., & Castelli, F. 1996, A&A, 314, 191
- Gray, D. F. 2005, The Observation and Analysis of Stellar Photospheres
- Hatzes, A. P., Guenther, E. W., Endl, M., et al. 2005, A&A, 437, 743
- Hauck, B. & Mermilliod, M. 1998, A&AS, 129, 431
- Hekker, S. & Meléndez, J. 2007, A&A, 475, 1003
- Hekker, S., Reffert, S., Quirrenbach, A., et al. 2006, A&A, 454, 943
- Hinkle, K., Wallace, L., Valenti, J., & Harmer, D. 2000, Visible and Near Infrared Atlas of the Arcturus Spectrum 3727-9300 A
- Høg, E., Fabricius, C., Makarov, V. V., et al. 2000, A&A, 355, L27
- Holmberg, J., Nordström, B., & Andersen, J. 2009, A&A, 501, 941
- Ida, S. & Lin, D. N. C. 2004, The Astrophysical Journal, 604, 388
- Jenkins, J. S., Jones, H. R. A., Pavlenko, Y., et al. 2008, A&A, 485, 571
- Jenkins, J. S., Jones, H. R. A., Tuomi, M., et al. 2017, MNRAS, 466, 443
- Jiang, C., Bedding, T. R., Stassun, K. G., et al. 2020, ApJ, 896, 65
- Jofré, E., Petrucci, R., Saffe, C., et al. 2015, A&A, 574, A50
- Jofré, P., Heiter, U., Soubiran, C., et al. 2014, A&A, 564, A133
- Johnson, J. A., Clanton, C., Howard, A. W., et al. 2011, The Astrophysical Journal Supplement Series, 197, 26
- Johnson, J. A., Fischer, D. A., Marcy, G. W., et al. 2007, ApJ, 665, 785
- Johnson, J. A., Morton, T. D., & Wright, J. T. 2013, ApJ, 763, 53
- Jones, M. I., Brahm, R., Wittenmyer, R. A., et al. 2017, A&A, 602, A58
- Jones, M. I., Jenkins, J. S., Bluhm, P., Rojo, P., & Melo, C. H. F. 2014, A&A, 566, A113
- Jones, M. I., Jenkins, J. S., Brahm, R., et al. 2016, A&A, 590, A38
- Jones, M. I., Jenkins, J. S., Rojo, P., & Melo, C. H. F. 2011, A&A, 536, A71
- Jones, M. I., Jenkins, J. S., Rojo, P., Melo, C. H. F., & Bluhm, P. 2013, A&A, 556, A78
- Jones, M. I., Jenkins, J. S., Rojo, P., Melo, C. H. F., & Bluhm, P. 2015a, A&A, 573, A3
- Jones, M. I., Jenkins, J. S., Rojo, P., Olivares, F., & Melo, C. H. F. 2015b, A&A, 580, A14
- Jones, M. I., Wittenmyer, R., Aguilera-Gómez, C., et al. 2020, arXiv e-prints, arXiv:2006.01277
- Kaufer, A., Stahl, O., Tubbesing, S., et al. 1999, The Messenger, 95, 8
- Kirby, E. N., Guhathakurta, P., Bolte, M., Sneden, C., & Geha, M. C. 2009, ApJ, 705, 328
- Kjeldsen, H. & Bedding, T. R. 1995, A&A, 293, 87
- Koen, C., Killick, D., van Wyk, F., & Marang, F. 2010, MNRAS, 403, 1949
- Kunitomo, M., Ikoma, M., Sato, B., Katsuta, Y., & Ida, S. 2011, ApJ, 737, 66
- Lagrange, A. M., Desort, M., Galland, F., Udry, S., & Mayor, M. 2009, A&A, 495, 335
- Lloyd, J. P. 2011, ApJ, 739, L49
- Lloyd, J. P. 2013, ApJ, 774, L2
- Luck, R. E. & Heiter, U. 2007, AJ, 133, 2464
- Maldonado, J., Villaver, E., & Eiroa, C. 2013, A&A, 554, A84
- Monaco, L., Bellazzini, M., Bonifacio, P., et al. 2005, A&A, 441, 141
- Montet, B. T., Morton, T. D., Foreman-Mackey, D., et al. 2015, ApJ, 809, 25
- Morel, T., Miglio, A., Lagarde, N., et al. 2014, A&A, 564, A119
- Mortier, A., Santos, N. C., Sousa, S. G., et al. 2013, A&A, 557, A70
- Morton, T. D. 2015, isochrones: Stellar model grid package, Astrophysics Source Code Library
- Mucciarelli, A. & Bonifacio, P. 2020, arXiv e-prints, arXiv:2003.07390
- Niedzielski, A., Konacki, M., Wolszczan, A., et al. 2007, ApJ, 669, 1354
- North, T. S. H., Campante, T. L., Miglio, A., et al. 2017, MNRAS, 472, 1866
- Pasquini, L., Döllinger, M. P., Weiss, A., et al. 2007, A&A, 473, 979
- Paxton, B., Bildsten, L., Dotter, A., et al. 2010, The Astrophysical Journal Supplement Series, 192, 3
- Perryman, M. A. C., Lindegren, L., Kovalevsky, J., et al. 1997, A&A, 500, 501
- Pinsonneault, M. H., Elsworth, Y. P., Tayar, J., et al. 2018, ApJS, 239, 32
- Rains, A. D., Ireland, M. J., White, T. R., Casagrande, L., & Karovicova, I. 2020, MNRAS, 493, 2377
- Reffert, S., Bergmann, C., Quirrenbach, A., Trifonov, T., & Künstler, A. 2015, A&A, 574, A116
- Ribas, Á., Bouy, H., & Merín, B. 2015, A&A, 576, A52
- Royer, F., Zorec, J., & Gómez, A. E. 2007, A&A, 463, 671
- Santos, N. C., Israelian, G., Mayor, M., Rebolo, R., & Udry, S. 2003, A&A, 398, 363
- Santos, N. C., Sousa, S. G., Mortier, A., et al. 2013, A&A, 556, A150
- Sato, B., Kambe, E., Takeda, Y., et al. 2005a, PASJ, 57, 97
- Sato, B., Kambe, E., Takeda, Y., et al. 2005b, PASJ, 57, 97
- Sato, B., Omiya, M., Harakawa, H., et al. 2012, PASJ, 64, 135
- Schlaufman, K. C. & Winn, J. N. 2013, ApJ, 772, 143
- Schrijver, C. J. & Pols, O. R. 1993, A&A, 278, 51
- Serenelli, A., Weiss, A., Aerts, C., et al. 2020, arXiv e-prints, arXiv:2006.10868
- Sestito, P., Bragaglia, A., Randich, S., et al. 2006, A&A, 458, 121
- Setiawan, J., Pasquini, L., da Silva, L., von der Lüh, O., & Hatzes, A. 2003, A&A, 397, 1151
- Silva Aguirre, V., Christensen-Dalsgaard, J., Cassisi, S., et al. 2020, A&A, 635, A164
- Silva Aguirre, V., Davies, G. R., Basu, S., et al. 2015, Monthly Notices of the Royal Astronomical Society, 452, 2127
- Silva Aguirre, V. & Serenelli, A. M. 2016, Astronomische Nachrichten, 337, 823
- Slumstrup, D., Grundahl, F., Silva Aguirre, V., & Brogaard, K. 2019, A&A, 622, A111
- Sneden, C. A. 1973, PhD thesis, THE UNIVERSITY OF TEXAS AT AUSTIN.
- Soderblom, D. R. 2010, Annual Review of Astronomy and Astrophysics, 48, 581
- Soto, M. G. & Jenkins, J. S. 2018, A&A, 615, A76
- Sousa, S. G., Adibekyan, V., Delgado-Mena, E., et al. 2018, A&A, 620, A58
- Sousa, S. G., Santos, N. C., Israelian, G., Mayor, M., & Monteiro, M. J. P. F. G. 2007, A&A, 469, 783
- Sousa, S. G., Santos, N. C., Mortier, A., et al. 2015, A&A, 576, A94
- Stassun, K. G. & Torres, G. 2018, ApJ, 862, 61
- Stock, S., Reffert, S., & Quirrenbach, A. 2018, A&A, 616, A33
- Takeda, Y. & Tajitsu, A. 2015, Monthly Notices of the Royal Astronomical Society, 450, 397
- Tokovinin, A., Fischer, D. A., Bonati, M., et al. 2013, PASP, 125, 1336

- Trifonov, T., Reffert, S., Tan, X., Lee, M. H., & Quirrenbach, A. 2014, *A&A*, 568, A64
- Tsantaki, M., Santos, N. C., Sousa, S. G., et al. 2019, *MNRAS*, 485, 2772
- Tsantaki, M., Sousa, S. G., Adibekyan, V. Z., et al. 2013, *A&A*, 555, A150
- Ulrich, R. K. 1986, *ApJ*, 306, L37
- Valenti, J. A. & Fischer, D. A. 2005, *ApJS*, 159, 141
- van Leeuwen, F. 2007, *A&A*, 474, 653
- Vanzi, L., Zapata, A., Flores, M., et al. 2018, *MNRAS*, 477, 5041
- Villaver, E. & Livio, M. 2009, *ApJ*, 705, L81
- Villaver, E., Livio, M., Mustill, A. J., & Siess, L. 2014, *The Astrophysical Journal*, 794, 3
- Vogt, S. S., Allen, S. L., Bigelow, B. C., et al. 1994, in *Society of Photo-Optical Instrumentation Engineers (SPIE) Conference Series*, Vol. 2198, *Instrumentation in Astronomy VIII*, ed. D. L. Crawford & E. R. Craine, 362
- Wittenmyer, R. A., Butler, R. P., Wang, L., et al. 2016a, *MNRAS*, 455, 1398
- Wittenmyer, R. A., Endl, M., Wang, L., et al. 2011, *ApJ*, 743, 184
- Wittenmyer, R. A., Johnson, J. A., Butler, R. P., et al. 2016b, *ApJ*, 818, 35
- Wittenmyer, R. A., Jones, M. I., Zhao, J., et al. 2017, *AJ*, 153, 51
- Wittenmyer, R. A., Liu, F., Wang, L., et al. 2016, *The Astronomical Journal*, 152, 19

Appendix A: Equivalent Width computation

The equivalent widths (EWs) were computed using the `EWComputation` module inside `SPECIES`⁹. For each line at wavelength λ in a given linelist, this module: 1) selects a region within 3 Å from the line and normalises the spectrum; 2) detects the absorption lines within the region; 3) fits a Gaussian-like profile to the line; and 4) computes the equivalent width of the line based on the fit parameters, and its corresponding uncertainty. Steps 1) and 2) were written following the prescription from Sousa et al. (2007).

Appendix A.1: Continuum normalization

The continuum normalization is done by fitting 2nd degree polynomials to the data, and rejecting the points that lie further than $rejt$ from the polynomial. The value $rejt$ was first introduced in Sousa et al. (2007), and is defined in `SPECIES` as $rejt = 1 - 1/\text{SNR}$, where SNR is the signal-to-noise ratio of the line region. The SNR is typically taken from the headers of the spectra, and it can be a global value, representing the whole spectrum, or have different values depending on the wavelength of the data.

Appendix A.2: Line detection

The detection of spectral lines is done by identifying the regions in the spectrum where the derivative is zero, and where the 2nd degree derivative is positive, indicating that the point corresponds to a local minimum. Before doing the derivations, the spectrum is smoothed by taking the convolution with a Box Kernel of size 4, and only the points with flux < -0.02 are considered as spectral lines. This is done to deal with very noisy data, where fluctuations in the continuum can be mistaken as line profiles. This will result in a set of N lines centred at wavelengths μ_i , where $i = 1, \dots, N$. We additionally define the index l which refers to the line closest to the target point, as defined by the criterion $\mu_l = \text{MIN}\{|\mu_i - \lambda|\}$.

Appendix A.3: Line profile fit

Once the N absorption lines are identified, we assume that each line follows a Gaussian-shaped profile, centered at wavelengths μ_i . The spectrum S at wavelength w can then be written as:

$$S(w) = \sum_{i=1}^N A_i \exp[-(w - \mu_i)^2 / 2\sigma_i^2]. \quad (\text{A.1})$$

We use the Scipy implementation of the Orthogonal Distance Regression (ODR, Boggs & Rogers 1990) method¹⁰ to minimize the above expression and estimate the values A_i , μ_i , and σ_i that best represent each line, with its corresponding uncertainties e_{A_i} , e_{μ_i} , and e_{σ_i} . The fit for the central line l is accepted if $w_l - \lambda \leq 0.15$ Å, $A_l \leq 0$ (absorption feature), $\sigma_l < 0.15$ Å, and the uncertainties for all the parameters is less than 0.12 dex. Otherwise, the line is discarded from the computation.

Line profiles fitted using our method are shown in Figure A.1.

⁹ Also available on its own at <https://github.com/msotov/EWComputation>

¹⁰ <https://docs.scipy.org/doc/scipy/reference/odr.html>

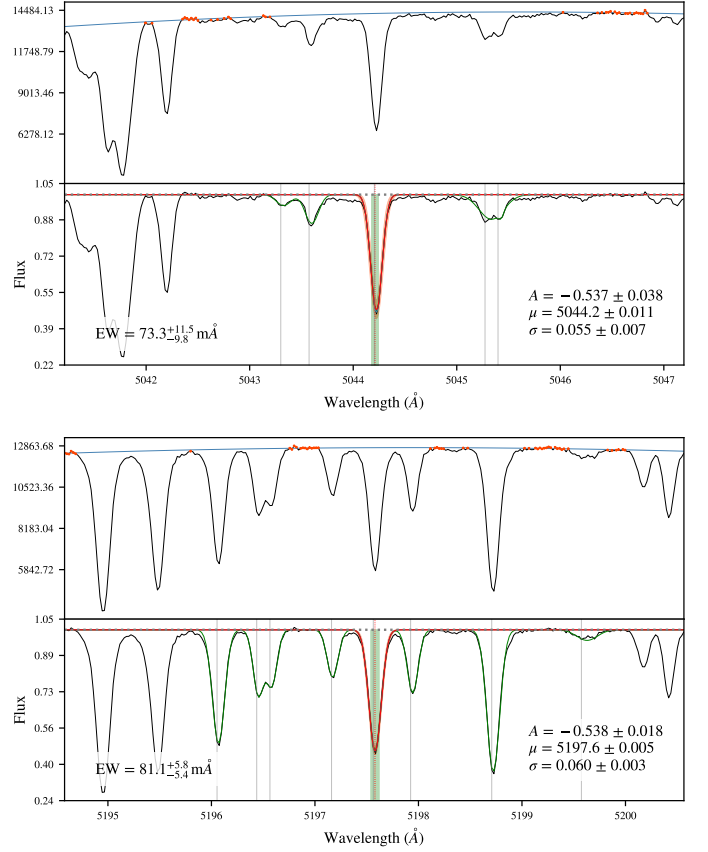


Fig. A.1. Fit performed to the Fe I 5044.21 Å and Fe II 5197.58 Å lines from one of the Sun spectra obtained by observing Ceres with HIRES. The gray lines are the absorption lines detected in the spectral range, and the green line the global fit to the data. The red region corresponds to the fit of the line l with its uncertainty, derived using the Gaussian parameters plus their uncertainties (quoted in the text). The green block represents the equivalent width.

Table A.1. Mean (μ), error in the mean (σ_μ), and standard deviation (σ) of the difference between the EWs computed by `SPECIES`, and from Bedell et al. (2017).

Star name	μ (mas)	σ_μ (mas)	σ (mas)
Ceres	-0.19	1.16	1.69
HD 191069	-0.14	2.78	4.11
HD 176733	-0.07	2.61	2.54
Kepler 11	0.09	2.73	4.29
HD 28474	0.08	0.73	1.09
HD 21774	-0.27	2.44	3.69
HD 16623	0.26	1.83	1.80
HD 1178	0.02	1.66	2.41

Appendix A.4: Equivalent width estimation

For each line l , the equivalent width is computed by integrating the line profile with parameters A_l , w_l , and σ_l , over the spectral region surrounding the line. The uncertainty in this value is estimated by changing the Gaussian parameters of the fit within 1σ of their uncertainty, and then selecting the 16% and 84% percentiles of the distribution.

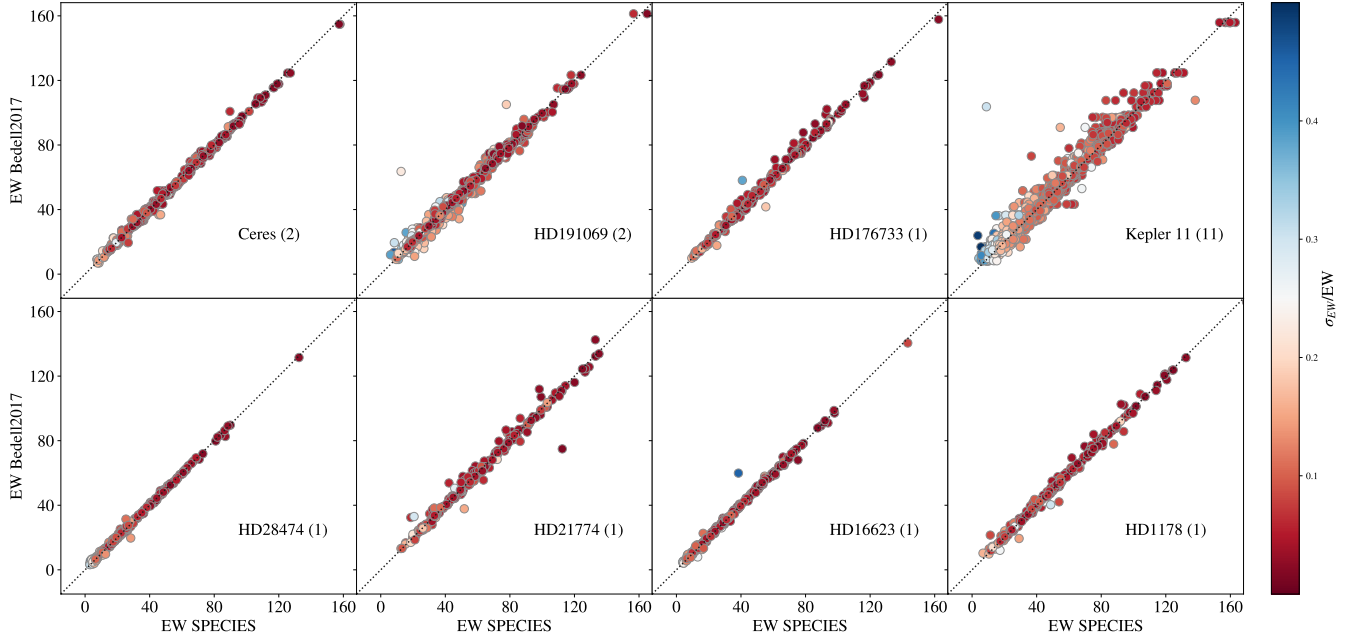


Fig. A.2. Comparison between the equivalent widths computed using SPECIES, against the values from [Bedell et al. \(2017\)](#). The number next to the names corresponds to the number of spectra available for each star. The color represents the uncertainty in the EW obtained with our method.

In order to assess the reliability of our method, we used it to estimate the equivalent width of the Sun, plus other 7 stars considered to be solar twins, and compared them to the values obtained by [Bedell et al. \(2017\)](#), where the continuum estimation and line profile fitting were performed for each line by hand using the *splot* module of IRAF¹¹. The results of our comparison, for the 8 stars, is shown in Figure A.2, and Table A.4. The spectra were taken with the HIRES spectrograph ([Vogt et al. 1994](#)), and we used the same line list as in [Bedell et al. \(2017\)](#).

Appendix B: Supplementary figures and tables

¹¹ IRAF is distributed by the National Optical Astronomy Observatories, which are operated by the Association of Universities for Research in Astronomy, Inc., under cooperative agreement with the National Science Foundation.

Table B.1. Line list used in the atmospheric parameters derivation.

λ (Å)	χ_I	$\log gf$	Element	λ (Å)	χ_I	$\log gf$	Element
5494.47	4.07	-1.96	Fe I	6151.62	2.18	-3.26	Fe I
5522.45	4.21	-1.47	Fe I	6157.73	4.07	-1.26	Fe I
5539.29	3.64	-2.59	Fe I	6165.36	4.14	-1.48	Fe I
5560.22	4.43	-1.1	Fe I	6173.34	2.22	-2.84	Fe I
5608.98	4.21	-2.31	Fe I	6188.0	3.94	-1.6	Fe I
5611.36	3.63	-2.93	Fe I	6200.32	2.61	-2.39	Fe I
5618.64	4.21	-1.34	Fe I	6213.44	2.22	-2.54	Fe I
5619.61	4.39	-1.49	Fe I	6219.29	2.2	-2.39	Fe I
5635.83	4.26	-1.59	Fe I	6226.74	3.88	-2.08	Fe I
5650.0	5.1	-0.8	Fe I	6232.65	3.65	-1.21	Fe I
5652.33	4.26	-1.77	Fe I	6240.65	2.22	-3.23	Fe I
5701.56	2.56	-2.16	Fe I	6246.33	3.6	-0.73	Fe I
5717.84	4.28	-0.98	Fe I	6252.57	2.4	-1.64	Fe I
5731.77	4.26	-1.1	Fe I	6265.14	2.18	-2.51	Fe I
5738.24	4.22	-2.24	Fe I	6270.23	2.86	-2.55	Fe I
5741.86	4.26	-1.69	Fe I	6280.62	0.86	-4.34	Fe I
5752.04	4.55	-0.92	Fe I	6297.8	2.22	-2.7	Fe I
5760.36	3.64	-2.46	Fe I	6301.51	3.65	-0.72	Fe I
5775.09	4.22	-1.11	Fe I	6311.5	2.83	-3.16	Fe I
5778.46	2.59	-3.44	Fe I	6315.81	4.07	-1.67	Fe I
5793.92	4.22	-1.62	Fe I	6322.69	2.59	-2.38	Fe I
5806.73	4.61	-0.93	Fe I	6330.85	4.73	-1.22	Fe I
5814.82	4.28	-1.81	Fe I	6335.34	2.2	-2.28	Fe I
5835.11	4.26	-2.18	Fe I	6380.75	4.19	-1.34	Fe I
5837.7	4.29	-2.3	Fe I	6481.88	2.28	-2.94	Fe I
5859.6	4.55	-0.63	Fe I	6498.95	0.96	-4.66	Fe I
5862.37	4.55	-0.42	Fe I	6518.37	2.83	-2.56	Fe I
5902.48	4.59	-1.86	Fe I	6533.94	4.56	-1.28	Fe I
5905.68	4.65	-0.78	Fe I	6574.25	0.99	-4.96	Fe I
5927.8	4.65	-1.07	Fe I	6581.22	1.48	-4.68	Fe I
5929.68	4.55	-1.16	Fe I	6593.88	2.43	-2.3	Fe I
5930.19	4.65	-0.34	Fe I	6608.04	2.28	-3.96	Fe I
5934.67	3.93	-1.08	Fe I	6609.12	2.56	-2.65	Fe I
5956.71	0.86	-4.56	Fe I	6627.56	4.55	-1.5	Fe I
5976.79	3.94	-1.3	Fe I	6633.76	4.56	-0.81	Fe I
5984.83	4.73	-0.29	Fe I	6667.72	4.58	-2.1	Fe I
6003.02	3.88	-1.02	Fe I	6703.58	2.76	-3.0	Fe I
6007.97	4.65	-0.76	Fe I	6713.75	4.79	-1.41	Fe I
6008.57	3.88	-0.92	Fe I	6725.36	4.1	-2.21	Fe I
6027.06	4.07	-1.2	Fe I	6726.67	4.61	-1.05	Fe I
6056.01	4.73	-0.46	Fe I	6733.15	4.64	-1.44	Fe I
6065.49	2.61	-1.49	Fe I	6739.52	1.56	-4.85	Fe I
6078.5	4.79	-0.38	Fe I	6745.97	4.07	-2.71	Fe I
6079.02	4.65	-0.97	Fe I	6750.16	2.42	-2.58	Fe I
6082.72	2.22	-3.53	Fe I	5197.58	3.23	-2.23	Fe II
6089.57	5.02	-0.87	Fe I	5234.63	3.22	-2.22	Fe II
6093.65	4.61	-1.32	Fe I	5991.38	3.15	-3.55	Fe II
6094.38	4.65	-1.56	Fe I	6369.46	2.89	-4.21	Fe II
6096.67	3.98	-1.76	Fe I	6416.93	3.89	-2.7	Fe II
6098.25	4.56	-1.81	Fe I	6456.39	3.9	-2.1	Fe II
6137.0	2.2	-2.91	Fe I	6516.08	2.89	-3.38	Fe II

Table B.2. Parameters derived with SPECIES for the stars included in interferometric and asteroseismology works. Some stars in the list do not belong to the EXPRESS program, but were included just to test the method.

HIP	HD	logg (cgs)	Radius (R_{\odot})	Mass (M_{\odot})	Age (Gyr)	References
343	225197	2.44 ± 0.12	$11.21^{+0.22}_{-0.13}$	$1.38^{+0.15}_{-0.14}$	$3.26^{+1.21}_{-0.86}$	7
655	344	2.36 ± 0.11	$11.25^{+0.41}_{-0.17}$	$1.27^{+0.16}_{-0.18}$	$4.24^{+2.49}_{-1.28}$	7
3137	3750	2.38 ± 0.13	$9.97^{+0.09}_{-0.08}$	$1.61^{+0.12}_{-0.13}$	$1.99^{+0.55}_{-0.38}$	1
4293	5457	2.69 ± 0.09	$9.07^{+0.24}_{-0.22}$	$1.50^{+0.12}_{-0.12}$	$2.47^{+0.73}_{-0.51}$	7
4587	5722	2.69 ± 0.08	$10.58^{+0.31}_{-0.31}$	$2.07^{+0.16}_{-0.21}$	$1.11^{+0.17}_{-0.23}$	1
8102	10700	4.33 ± 0.06	$0.83^{+0.01}_{-0.01}$	$0.77^{+0.01}_{-0.01}$	$13.04^{+0.34}_{-0.73}$	3, 5
8928	11977	2.72 ± 0.08	$10.64^{+0.23}_{-0.20}$	$2.29^{+0.15}_{-0.12}$	$0.82^{+0.15}_{-0.17}$	1
9440	12438	2.65 ± 0.08	$9.82^{+0.29}_{-0.23}$	$1.86^{+0.08}_{-0.03}$	$1.09^{+0.05}_{-0.04}$	1
10234	13468	2.64 ± 0.08	$10.57^{+0.32}_{-0.29}$	$2.00^{+0.19}_{-0.17}$	$1.19^{+0.15}_{-0.23}$	1
11791	15779	2.75 ± 0.10	$9.90^{+0.27}_{-0.24}$	$2.18^{+0.15}_{-0.16}$	$1.03^{+0.20}_{-0.23}$	1
13147	17652	2.56 ± 0.08	$10.15^{+0.11}_{-0.10}$	$1.87^{+0.04}_{-0.06}$	$1.16^{+8.17}_{-0.02}$	1
16537	22049	4.40 ± 0.06	$0.72^{+0.00}_{-0.00}$	$0.80^{+0.01}_{-0.01}$	$0.59^{+0.92}_{-0.38}$	3
19849	26965	4.33 ± 0.06	$0.77^{+0.03}_{-0.02}$	$0.75^{+0.02}_{-0.02}$	$12.18^{+0.99}_{-2.15}$	3
69673	124897	1.67 ± 0.10	$24.76^{+1.28}_{-1.13}$	$0.91^{+0.09}_{-0.06}$	$9.87^{+2.42}_{-2.67}$	2
79672	146233	4.36 ± 0.05	$1.04^{+0.02}_{-0.02}$	$1.03^{+0.03}_{-0.03}$	$3.92^{+1.58}_{-1.56}$	3
89962	168723	3.01 ± 0.08	$5.54^{+0.07}_{-0.06}$	$1.57^{+0.08}_{-0.08}$	$1.89^{+0.29}_{-0.23}$	2
92968	175679	2.88 ± 0.10	$12.63^{+0.49}_{-0.48}$	$3.04^{+0.07}_{-0.26}$	$0.35^{+0.10}_{-0.02}$	2
95124	181342	3.13 ± 0.10	$5.31^{+0.06}_{-0.06}$	$1.64^{+0.09}_{-0.09}$	$2.00^{+0.37}_{-0.27}$	8
95222	181907	2.43 ± 0.10	$11.20^{+0.22}_{-0.13}$	$1.45^{+0.17}_{-0.14}$	$2.68^{+0.93}_{-0.74}$	2
98036	188512	3.61 ± 0.07	$3.00^{+0.02}_{-0.02}$	$1.37^{+0.03}_{-0.03}$	$3.02^{+0.14}_{-0.11}$	2, 5
102014	196737	2.71 ± 0.11	$9.89^{+0.32}_{-0.29}$	$1.48^{+0.12}_{-0.14}$	$2.61^{+0.96}_{-0.58}$	7
103836	200073	2.75 ± 0.09	$7.84^{+0.21}_{-0.20}$	$1.03^{+0.09}_{-0.07}$	$8.79^{+2.32}_{-2.04}$	7
105854	203949	2.46 ± 0.16	$10.75^{+0.22}_{-0.16}$	$0.97^{+0.09}_{-0.04}$	$11.50^{+1.40}_{-2.58}$	4, 7
110813	212771	3.38 ± 0.07	$4.33^{+0.04}_{-0.04}$	$1.57^{+0.06}_{-0.07}$	$1.95^{+0.25}_{-0.17}$	4, 8
114775	219263	2.70 ± 0.12	$8.62^{+0.27}_{-0.25}$	$1.43^{+0.13}_{-0.12}$	$3.26^{+1.16}_{-0.78}$	7
116630	222076	3.17 ± 0.12	$4.28^{+0.05}_{-0.05}$	$1.28^{+0.09}_{-0.09}$	$4.54^{+1.20}_{-0.92}$	6

References. (1) Gallenne et al. (2018); (2) Morel et al. (2014); (3) Tsantaki et al. (2013); (4) Campante et al. (2019); (5) Rains et al. (2020); (6) Jiang et al. (2020); (7) Aguirre et al. (2020); (8) North et al. (2017).

Table B.3. Literature data for stars used in the comparison with interferometry and asteroseismology. Only the quantities plotted in Figures 2 and 3 are listed.

HIP	log g (cgs)	Radius (R_{\odot})	Mass (M_{\odot})	Age (Gyr)	Reference
343	2.54 ± 0.07^a	10.69 ± 0.52	1.44 ± 0.18	3.50 ± 1.05	Aguirre et al. (2020)^b
655	2.41 ± 0.09^a	11.27 ± 0.77	1.19 ± 0.17	6.80 ± 3.11	Aguirre et al. (2020)^b
3137		10.52 ± 0.24			Gallenne et al. (2018)
4293	2.58 ± 0.05^a	9.30 ± 0.32	1.19 ± 0.11	5.90 ± 1.82	Aguirre et al. (2020)^b
4587		10.91 ± 0.28			Gallenne et al. (2018)
8102		0.79 ± 0.00^c			Tsantaki et al. (2013)
		0.80 ± 0.00			Rains et al. (2020)
8928		11.17 ± 0.15			Gallenne et al. (2018)
9440		10.59 ± 0.32			Gallenne et al. (2018)
10234		11.17 ± 0.21			Gallenne et al. (2018)
11791		10.57 ± 0.17			Gallenne et al. (2018)
13147		10.45 ± 0.17			Gallenne et al. (2018)
16537		0.74 ± 0.01^c			Tsantaki et al. (2013)
19849		0.81 ± 0.00^c			Tsantaki et al. (2013)
69673	1.42 ± 0.08				Morel et al. (2014)
79672		1.03 ± 0.01^c			Tsantaki et al. (2013)
89962	3.00 ± 0.05				Morel et al. (2014)
92968	2.66 ± 0.11				Morel et al. (2014)
95124	3.24 ± 0.04^a	$5.23^{+0.25}_{-0.18}$	$1.73^{+0.18}_{-0.13}$	$1.69^{+0.47}_{-0.41}$	North et al. (2017)
95222	2.35 ± 0.04				Morel et al. (2014)
98036		3.06 ± 0.02			Rains et al. (2020)
	3.53 ± 0.04				Morel et al. (2014)
102014	2.57 ± 0.09^a	10.18 ± 0.76	1.40 ± 0.22	3.40 ± 1.32	Aguirre et al. (2020)^b
103836	2.66 ± 0.05^a	7.92 ± 0.30	1.04 ± 0.10	9.90 ± 2.59	Aguirre et al. (2020)^b
105854	2.42 ± 0.04	10.34 ± 0.55	1.00 ± 0.16	7.29 ± 3.06	Campante et al. (2019)^d
	2.42 ± 0.07^a	10.85 ± 0.65	1.13 ± 0.13	8.50 ± 3.33	Aguirre et al. (2020)^b
110813	3.29 ± 0.04^a	$4.53^{+0.13}_{-0.13}$	$1.46^{+0.09}_{-0.09}$	$2.46^{+0.67}_{-0.50}$	North et al. (2017)
	3.26 ± 0.01	4.61 ± 0.09	1.42 ± 0.07	2.90 ± 0.47	Campante et al. (2019)
114775	2.67 ± 0.10^a	9.00 ± 0.65	1.38 ± 0.23	4.50 ± 1.55	Aguirre et al. (2020)^b
116630	3.21 ± 0.05	4.34 ± 0.21	1.12 ± 0.12	7.40 ± 2.70	Jiang et al. (2020)

Notes. ^(a) Surface gravity was not listed in the literature, but were computed from the given masses and radius.

^(b) Uncertainties were computed by adding both values listed in [Aguirre et al. \(2020\)](#).

^(c) Radius were not given in [Tsantaki et al. \(2013\)](#), but were computed from the temperature, angular size, and distance.

^(d) We used the values corresponding to the Red Clump solution for this star, as it is the most favourable solution based on the arguments presented by the authors.

Table B.4. SPECIES results for the EXPRESS star sample. Only 40 lines are shown, with a subset of columns. Full version is available online.

Starname	Instrument	Temperature (K)	logg (cgs)	[Fe/H] (dex)	ξ_i (km s ⁻¹)	v _{ini} (km s ⁻¹)	Mass (M _⊙)	Radius (R _⊙)	log L (L _⊙)	Age (Gyr)	EEP	P _{RGB} ^a	P _{HB} ^b
HIP100062	FEROS	4933 ± 50	2.63 ± 0.09	-0.09 ± 0.06	1.44 ± 0.06	3.80 ± 0.55	1.86 ^{+0.10} _{-0.13}	10.75 ^{+0.26} _{-0.38}	1.770 ^{+0.013} _{-0.014}	1.36 ^{+0.22} _{-0.17}	658 ⁺⁶ ₋₃	0.01	0.99
HIP101477	FEROS	4956 ± 50	2.70 ± 0.11	-0.05 ± 0.06	1.50 ± 0.08	3.79 ± 0.57	2.08 ^{+0.20} _{-0.26}	10.48 ^{+0.38} _{-0.51}	1.770 ^{+0.014} _{-0.015}	1.18 ^{+0.13} _{-0.17}	668 ⁺⁵ ₋₃	0.01	0.99
HIP10164	FEROS	4871 ± 52	3.39 ± 0.10	0.12 ± 0.06	0.98 ± 0.13	3.17 ± 0.49	1.19 ^{+0.07} _{-0.07}	3.29 ^{+0.03} _{-0.03}	0.740 ^{+0.006} _{-0.007}	6.05 ^{+1.23} _{-1.05}	482 ⁺¹⁰ ₋₁	1.00	0.00
HIP101911	FEROS	4864 ± 50	2.85 ± 0.10	-0.05 ± 0.06	1.25 ± 0.09	3.36 ± 0.61	1.29 ^{+0.10} _{-0.19}	6.22 ^{+0.11} _{-0.19}	1.270 ^{+0.007} _{-0.011}	4.09 ^{+1.16} _{-0.85}	503 ⁺¹ ₋₁	1.00	0.00
HIP102014	CHIRON	4677 ± 50	2.71 ± 0.11	-0.07 ± 0.05	1.32 ± 0.09	3.68 ± 0.53	1.48 ^{+0.12} _{-0.14}	9.89 ^{+0.32} _{-0.32}	1.630 ^{+0.011} _{-0.015}	2.61 ^{+0.86} _{-0.38}	519 ⁺¹ ₋₁	1.00	0.00
HIP10234	FEROS	5002 ± 50	2.64 ± 0.08	-0.16 ± 0.05	1.46 ± 0.05	3.17 ± 0.65	1.70 ^{+0.17} _{-0.17}	13.30 ^{+0.32} _{-0.32}	1.900 ^{+0.017} _{-0.017}	1.19 ^{+0.38} _{-0.37}	665 ⁺⁵ ₋₃	0.00	1.00
HIP102773	CHIRON	4698 ± 50	2.58 ± 0.10	-0.09 ± 0.06	1.52 ± 0.07	4.38 ± 0.41	1.78 ^{+0.25} _{-0.18}	10.37 ^{+0.39} _{-0.39}	1.790 ^{+0.017} _{-0.017}	1.53 ^{+0.37} _{-0.37}	681 ⁺⁷ ₋₁₄₉	0.39	0.61
HIP10326	CHIRON	4922 ± 50	2.47 ± 0.11	-0.15 ± 0.06	1.42 ± 0.09	3.74 ± 0.59	1.63 ^{+0.19} _{-0.15}	11.36 ^{+0.25} _{-0.20}	1.820 ^{+0.013} _{-0.013}	1.84 ^{+0.31} _{-0.31}	668 ⁺² ₋₃	0.00	1.00
HIP103836	CHIRON	4636 ± 50	2.75 ± 0.09	-0.15 ± 0.05	1.18 ± 0.07	3.72 ± 0.51	1.03 ^{+0.09} _{-0.09}	7.84 ^{+0.21} _{-0.21}	1.420 ^{+0.013} _{-0.013}	8.79 ^{+0.42} _{-0.42}	512 ⁺¹ ₋₁	1.00	0.00
HIP104148	FEROS	4808 ± 55	2.56 ± 0.12	-0.05 ± 0.06	1.47 ± 0.10	5.02 ± 0.44	1.65 ^{+0.13} _{-0.13}	9.39 ^{+0.30} _{-0.30}	1.620 ^{+0.006} _{-0.006}	1.78 ^{+0.36} _{-0.36}	517 ⁺¹ ₋₁	0.94	0.06
HIP104838	FEROS	4911 ± 50	3.20 ± 0.09	0.00 ± 0.05	1.12 ± 0.09	2.71 ± 0.60	1.16 ^{+0.08} _{-0.08}	3.84 ^{+0.04} _{-0.04}	0.880 ^{+0.006} _{-0.006}	6.00 ^{+1.30} _{-1.30}	487 ⁺¹ ₋₁	1.00	0.00
HIP10548	FEROS	4993 ± 50	3.51 ± 0.11	0.01 ± 0.05	1.23 ± 0.10	2.87 ± 0.47	1.22 ^{+0.07} _{-0.07}	3.14 ^{+0.06} _{-0.06}	0.730 ^{+0.007} _{-0.007}	5.12 ^{+1.09} _{-0.79}	480 ⁺¹ ₋₁	1.00	0.00
HIP105854	FEROS	4687 ± 88	2.46 ± 0.16	0.16 ± 0.06	1.49 ± 0.16	4.76 ± 0.55	0.97 ^{+0.09} _{-0.09}	10.75 ^{+0.22} _{-0.22}	1.660 ^{+0.018} _{-0.018}	11.50 ^{+1.40} _{-1.40}	661 ⁺³ ₋₃	0.12	0.88
HIP105856	FEROS	4801 ± 62	3.05 ± 0.13	0.06 ± 0.05	1.07 ± 0.14	2.41 ± 0.46	1.29 ^{+0.16} _{-0.16}	4.99 ^{+0.06} _{-0.06}	1.090 ^{+0.008} _{-0.008}	4.40 ^{+1.28} _{-0.99}	495 ⁺¹ ₋₁	1.00	0.00
HIP106055	FEROS	4778 ± 65	2.45 ± 0.14	-0.02 ± 0.06	1.39 ± 0.12	3.94 ± 0.73	1.17 ^{+0.13} _{-0.13}	11.05 ^{+0.12} _{-0.12}	1.730 ^{+0.012} _{-0.012}	5.69 ^{+0.26} _{-0.26}	664 ⁺² ₋₃	0.00	1.00
HIP106922	FEROS	4803 ± 53	2.90 ± 0.11	0.01 ± 0.06	1.20 ± 0.10	3.34 ± 0.58	1.27 ^{+0.16} _{-0.16}	5.86 ^{+0.08} _{-0.08}	1.220 ^{+0.016} _{-0.016}	4.52 ^{+1.16} _{-0.84}	501 ⁺¹ ₋₁	1.00	0.00
HIP107122	FEROS	4965 ± 50	3.28 ± 0.09	0.06 ± 0.06	1.09 ± 0.09	2.88 ± 0.43	1.30 ^{+0.08} _{-0.08}	3.80 ^{+0.04} _{-0.04}	0.880 ^{+0.008} _{-0.008}	4.22 ^{+0.84} _{-0.84}	486 ⁺¹ ₋₁	1.00	0.00
HIP107773	FEROS	4942 ± 50	2.65 ± 0.11	-0.02 ± 0.06	1.47 ± 0.09	4.36 ± 0.56	2.26 ^{+0.18} _{-0.18}	11.20 ^{+0.29} _{-0.29}	1.830 ^{+0.008} _{-0.008}	0.97 ^{+0.26} _{-0.26}	676 ⁺² ₋₃	0.01	0.99
HIP108543	FEROS	5080 ± 50	2.50 ± 0.12	0.06 ± 0.06	1.64 ± 0.11	4.44 ± 0.59	3.03 ^{+0.08} _{-0.08}	16.26 ^{+0.41} _{-0.41}	2.170 ^{+0.018} _{-0.018}	0.40 ^{+0.04} _{-0.04}	681 ⁺³ ₋₃	0.01	0.99
HIP109228	FEROS	4993 ± 50	3.42 ± 0.07	-0.02 ± 0.05	1.02 ± 0.08	2.28 ± 0.56	1.19 ^{+0.07} _{-0.07}	3.21 ^{+0.03} _{-0.03}	0.750 ^{+0.009} _{-0.009}	5.47 ^{+1.07} _{-0.96}	481 ⁺¹ ₋₁	1.00	0.00
HIP110391	FEROS	4738 ± 50	2.54 ± 0.10	-0.23 ± 0.06	1.35 ± 0.07	3.25 ± 0.68	1.08 ^{+0.11} _{-0.11}	9.02 ^{+0.24} _{-0.24}	1.540 ^{+0.008} _{-0.008}	6.94 ^{+0.96} _{-0.96}	516 ⁺² ₋₂	1.00	0.00
HIP110529	FEROS	5113 ± 50	3.06 ± 0.11	0.09 ± 0.06	1.43 ± 0.09	3.63 ± 0.60	2.21 ^{+0.10} _{-0.10}	8.84 ^{+0.24} _{-0.24}	1.640 ^{+0.014} _{-0.014}	0.89 ^{+0.13} _{-0.13}	654 ⁺² ₋₁₂	0.16	0.84
HIP111515	CHIRON	4981 ± 50	2.85 ± 0.11	0.03 ± 0.06	1.37 ± 0.10	4.23 ± 0.49	2.08 ^{+0.03} _{-0.03}	8.32 ^{+0.07} _{-0.07}	1.570 ^{+0.007} _{-0.007}	1.03 ^{+0.06} _{-0.06}	643 ⁺¹ ₋₁	0.12	0.88
HIP111909	FEROS	4920 ± 54	3.11 ± 0.11	0.11 ± 0.06	1.19 ± 0.11	3.20 ± 0.66	1.36 ^{+0.09} _{-0.09}	4.29 ^{+0.04} _{-0.04}	0.980 ^{+0.004} _{-0.004}	3.77 ^{+0.03} _{-0.03}	490 ⁺¹ ₋₁	1.00	0.00
HIP113779	FEROS	5032 ± 50	3.55 ± 0.09	0.17 ± 0.05	1.00 ± 0.11	2.32 ± 0.54	1.50 ^{+0.05} _{-0.05}	3.57 ^{+0.03} _{-0.03}	0.850 ^{+0.008} _{-0.008}	2.73 ^{+0.33} _{-0.33}	483 ⁺¹ ₋₁	1.00	0.00
HIP114408	CHIRON	4875 ± 50	3.28 ± 0.07	-0.27 ± 0.05	0.92 ± 0.07	3.60 ± 0.47	1.07 ^{+0.07} _{-0.07}	4.69 ^{+0.04} _{-0.04}	1.060 ^{+0.009} _{-0.009}	6.98 ^{+1.23} _{-1.23}	495 ⁺¹ ₋₁	1.00	0.00
HIP114775	CHIRON	4668 ± 57	2.70 ± 0.12	0.10 ± 0.05	1.22 ± 0.12	4.48 ± 0.54	1.43 ^{+0.13} _{-0.13}	8.62 ^{+0.27} _{-0.27}	1.500 ^{+0.009} _{-0.009}	3.26 ^{+1.16} _{-0.78}	514 ⁺¹ ₋₁	1.00	0.00
HIP114933	FEROS	4823 ± 59	2.99 ± 0.12	0.06 ± 0.06	1.17 ± 0.12	3.33 ± 0.51	1.39 ^{+0.09} _{-0.09}	5.27 ^{+0.23} _{-0.23}	1.140 ^{+0.004} _{-0.004}	3.40 ^{+0.78} _{-0.78}	497 ⁺¹ ₋₁	1.00	0.00
HIP115620	CHIRON	4816 ± 50	2.77 ± 0.09	-0.00 ± 0.06	1.42 ± 0.07	4.13 ± 0.50	1.90 ^{+0.06} _{-0.06}	10.47 ^{+0.30} _{-0.30}	1.730 ^{+0.004} _{-0.004}	1.36 ^{+0.10} _{-0.10}	653 ⁺⁸ ₋₇	0.00	1.00
HIP115769	CHIRON	4961 ± 50	2.62 ± 0.12	-0.26 ± 0.06	1.58 ± 0.08	4.01 ± 0.56	1.24 ^{+0.08} _{-0.08}	10.80 ^{+0.15} _{-0.15}	1.770 ^{+0.006} _{-0.006}	3.94 ^{+1.98} _{-2.98}	664 ⁺³ ₋₃	0.04	0.96
HIP11600	FEROS	4969 ± 64	3.69 ± 0.14	0.18 ± 0.06	1.23 ± 0.10	2.89 ± 0.75	1.07 ^{+0.04} _{-0.04}	2.43 ^{+0.02} _{-0.02}	0.480 ^{+0.006} _{-0.006}	9.17 ^{+1.27} _{-0.97}	474 ⁺¹ ₋₁	1.00	0.00
HIP116630	FEROS	4878 ± 60	3.17 ± 0.12	0.08 ± 0.06	1.18 ± 0.12	2.99 ± 0.53	1.28 ^{+0.08} _{-0.08}	4.28 ^{+0.05} _{-0.05}	0.970 ^{+0.008} _{-0.008}	4.54 ^{+0.92} _{-0.92}	490 ⁺¹ ₋₁	1.00	0.00
HIP117314	CHIRON	4827 ± 50	2.39 ± 0.11	-0.05 ± 0.06	1.49 ± 0.10	4.21 ± 0.59	1.23 ^{+0.16} _{-0.16}	11.04 ^{+0.15} _{-0.15}	1.750 ^{+0.008} _{-0.008}	4.53 ^{+1.33} _{-1.33}	665 ⁺² ₋₃	0.00	1.00
HIP117411	FEROS	4828 ± 59	2.97 ± 0.12	0.06 ± 0.06	1.24 ± 0.12	3.12 ± 0.61	1.18 ^{+0.06} _{-0.06}	5.10 ^{+0.07} _{-0.07}	1.090 ^{+0.010} _{-0.010}	6.08 ^{+1.26} _{-1.26}	497 ⁺¹ ₋₁	1.00	0.00
HIP11791	FEROS	4958 ± 50	2.75 ± 0.10	-0.01 ± 0.06	1.42 ± 0.08	3.24 ± 0.50	2.18 ^{+0.16} _{-0.16}	9.90 ^{+0.32} _{-0.32}	1.730 ^{+0.014} _{-0.014}	1.03 ^{+0.26} _{-0.26}	665 ⁺³ ₋₃	0.00	1.00
HIP11867	CHIRON	4775 ± 51	2.55 ± 0.11	-0.02 ± 0.05	1.36 ± 0.09	4.67 ± 0.57	1.64 ^{+0.13} _{-0.13}	11.84 ^{+0.26} _{-0.26}	1.820 ^{+0.014} _{-0.014}	2.01 ^{+0.43} _{-0.43}	671 ⁺⁵ ₋₃	0.02	0.98
HIP1230	FEROS	4866 ± 51	2.87 ± 0.11	-0.13 ± 0.05	1.28 ± 0.09	3.67 ± 0.59	1.31 ^{+0.16} _{-0.16}	6.73 ^{+0.10} _{-0.10}	1.340 ^{+0.012} _{-0.012}	3.79 ^{+1.03} _{-0.75}	506 ⁺¹ ₋₁	1.00	0.00
HIP13147	FEROS	4888 ± 50	2.52 ± 0.07	-0.36 ± 0.05	1.50 ± 0.04	3.35 ± 0.62	0.89 ^{+0.03} _{-0.03}	10.08 ^{+0.13} _{-0.13}	1.730 ^{+0.012} _{-0.012}	10.09 ^{+1.18} _{-1.44}	667 ⁺¹ ₋₁	0.00	1.00
HIP16142	CHIRON	4752 ± 50	2.68 ± 0.10	0.05 ± 0.06	1.46 ± 0.09	4.24 ± 0.54	1.74 ^{+0.14} _{-0.14}	10.96 ^{+0.23} _{-0.23}	1.740 ^{+0.011} _{-0.011}	1.72 ^{+1.58} _{-0.89}	661 ⁺² ₋₁₀	0.04	0.96
HIP16780	CHIRON	5097 ± 50	2.80 ± 0.07	-0.26 ± 0.05	1.47 ± 0.04	4.03 ± 0.51	2.21 ^{+0.21} _{-0.14}	9.93 ^{+0.19} _{-0.19}	1.780 ^{+0.014} _{-0.014}	0.84 ^{+0.10} _{-0.17}	669 ⁺³ ₋₃	0.00	1.00

Notes. ^(a) Probability of the star being in the RGB. ^(b) Probability of the star being in the HB.

Table B.5. Results for the Sun spectra. Spectra labelled Sun01 to Sun07 were taken from Blanco-Cuaresma et al. (2014), while the rest were obtained through the ESO data archive. ATLAS refers to data from Hinkle et al. (2000), HARPS to Aurière (2003), and UVES to Dekker et al. (2000).

Starname	Instrument	[Fe/H] (dex)	Temperature (K)	logg (cgs)	ξ_t (km s ⁻¹)	v sin i (km s ⁻¹)	V _{mac} (km s ⁻¹)	Mass (M _⊙)	Radius (R _⊙)	log L (L _⊙)	Age (Gyr)
Sun0	ATLAS	-0.04 ± 0.05	5790 ± 50	4.40 ± 0.04	0.84 ± 0.04	2.82 ± 0.23	3.17 ± 0.22	0.97 ^{+0.03} _{-0.03}	1.02 ^{+0.05} _{-0.04}	0.03 ^{+0.04} _{-0.04}	5.94 ^{+1.37} _{-1.71}
Sun1	HARPS	-0.03 ± 0.05	5776 ± 50	4.38 ± 0.06	0.82 ± 0.06	3.51 ± 0.17	3.21 ± 0.16	0.97 ^{+0.03} _{-0.03}	1.05 ^{+0.07} _{-0.06}	0.04 ^{+0.06} _{-0.06}	6.64 ^{+2.76} _{-2.18}
Sun2	HARPS	-0.02 ± 0.05	5766 ± 50	4.34 ± 0.04	0.86 ± 0.05	3.61 ± 0.16	3.25 ± 0.16	0.97 ^{+0.03} _{-0.03}	1.10 ^{+0.06} _{-0.05}	0.08 ^{+0.05} _{-0.05}	8.01 ^{+1.40} _{-1.46}
Sun3	HARPS	-0.03 ± 0.05	5765 ± 50	4.35 ± 0.05	0.88 ± 0.05	3.83 ± 0.23	3.18 ± 0.23	0.97 ^{+0.03} _{-0.03}	1.08 ^{+0.06} _{-0.06}	0.06 ^{+0.06} _{-0.05}	7.73 ^{+1.35} _{-1.56}
Sun4	HARPS	-0.03 ± 0.05	5767 ± 50	4.36 ± 0.05	0.86 ± 0.05	3.60 ± 0.16	3.21 ± 0.16	0.97 ^{+0.03} _{-0.03}	1.07 ^{+0.06} _{-0.06}	0.05 ^{+0.05} _{-0.05}	7.34 ^{+1.56} _{-1.66}
Sun5	NARVAL	-0.05 ± 0.05	5759 ± 50	4.45 ± 0.09	0.84 ± 0.10	3.77 ± 0.28	2.97 ± 0.26	0.96 ^{+0.03} _{-0.03}	0.97 ^{+0.06} _{-0.06}	-0.03 ^{+0.08} _{-0.06}	4.76 ^{+2.96} _{-2.95}
Sun6	NARVAL	-0.02 ± 0.05	5780 ± 50	4.38 ± 0.05	0.84 ± 0.05	3.42 ± 0.17	3.23 ± 0.16	0.97 ^{+0.03} _{-0.03}	1.05 ^{+0.06} _{-0.06}	0.04 ^{+0.06} _{-0.05}	6.65 ^{+1.65} _{-1.74}
Sun7	UVES	-0.03 ± 0.05	5794 ± 50	4.40 ± 0.05	0.87 ± 0.05	3.14 ± 0.24	3.18 ± 0.23	0.98 ^{+0.03} _{-0.03}	1.02 ^{+0.06} _{-0.05}	0.03 ^{+0.05} _{-0.05}	5.81 ^{+1.67} _{-1.99}
ceres01	HARPS	-0.03 ± 0.05	5757 ± 50	4.33 ± 0.08	0.78 ± 0.10	3.56 ± 0.26	3.18 ± 0.25	0.97 ^{+0.03} _{-0.03}	1.08 ^{+0.10} _{-0.09}	0.06 ^{+0.08} _{-0.08}	7.96 ^{+2.44} _{-1.63}
ceres02	HARPS	-0.02 ± 0.05	5783 ± 50	4.41 ± 0.05	0.77 ± 0.06	3.54 ± 0.16	3.19 ± 0.16	0.98 ^{+0.03} _{-0.03}	1.02 ^{+0.06} _{-0.06}	0.02 ^{+0.05} _{-0.05}	5.74 ^{+1.76} _{-1.44}
ceres03	HARPS	-0.04 ± 0.05	5756 ± 50	4.34 ± 0.06	0.81 ± 0.07	3.43 ± 0.24	3.16 ± 0.24	0.96 ^{+0.03} _{-0.03}	1.08 ^{+0.08} _{-0.07}	0.06 ^{+0.07} _{-0.06}	7.96 ^{+1.58} _{-1.99}
moon	HARPS	-0.02 ± 0.05	5761 ± 50	4.39 ± 0.06	0.81 ± 0.06	3.92 ± 0.23	3.08 ± 0.23	0.97 ^{+0.03} _{-0.03}	1.02 ^{+0.07} _{-0.06}	0.02 ^{+0.06} _{-0.06}	6.37 ^{+2.89} _{-2.29}
ganymede	HARPS	-0.03 ± 0.05	5777 ± 50	4.36 ± 0.05	0.86 ± 0.05	3.59 ± 0.16	3.24 ± 0.16	0.97 ^{+0.03} _{-0.03}	1.07 ^{+0.06} _{-0.05}	0.06 ^{+0.05} _{-0.05}	7.14 ^{+2.49} _{-1.69}
sun01	HARPS	-0.04 ± 0.05	5752 ± 50	4.32 ± 0.05	0.68 ± 0.08	3.70 ± 0.23	3.17 ± 0.23	0.96 ^{+0.03} _{-0.03}	1.10 ^{+0.07} _{-0.07}	0.08 ^{+0.06} _{-0.06}	8.54 ^{+2.64} _{-1.43}
sun02	HARPS	-0.00 ± 0.05	5893 ± 64	4.47 ± 0.12	0.65 ± 0.19	3.61 ± 0.35	3.44 ± 0.35	1.02 ^{+0.03} _{-0.03}	1.01 ^{+0.11} _{-0.08}	0.05 ^{+0.09} _{-0.08}	3.23 ^{+2.10} _{-2.10}
sun03	HARPS	-0.04 ± 0.05	5791 ± 50	4.36 ± 0.07	0.65 ± 0.10	3.74 ± 0.24	3.25 ± 0.24	0.98 ^{+0.03} _{-0.03}	1.06 ^{+0.08} _{-0.07}	0.05 ^{+0.07} _{-0.07}	6.71 ^{+2.40} _{-2.40}
sun04	HARPS	-0.04 ± 0.05	5743 ± 50	4.25 ± 0.07	0.75 ± 0.09	3.68 ± 0.24	3.28 ± 0.24	0.96 ^{+0.03} _{-0.03}	1.19 ^{+0.10} _{-0.09}	0.14 ^{+0.08} _{-0.07}	9.64 ^{+1.37} _{-1.32}
sun05	HARPS	-0.04 ± 0.05	5772 ± 50	4.36 ± 0.08	0.65 ± 0.12	3.68 ± 0.25	3.19 ± 0.25	0.97 ^{+0.03} _{-0.03}	1.07 ^{+0.08} _{-0.08}	0.05 ^{+0.08} _{-0.07}	7.42 ^{+2.64} _{-2.64}

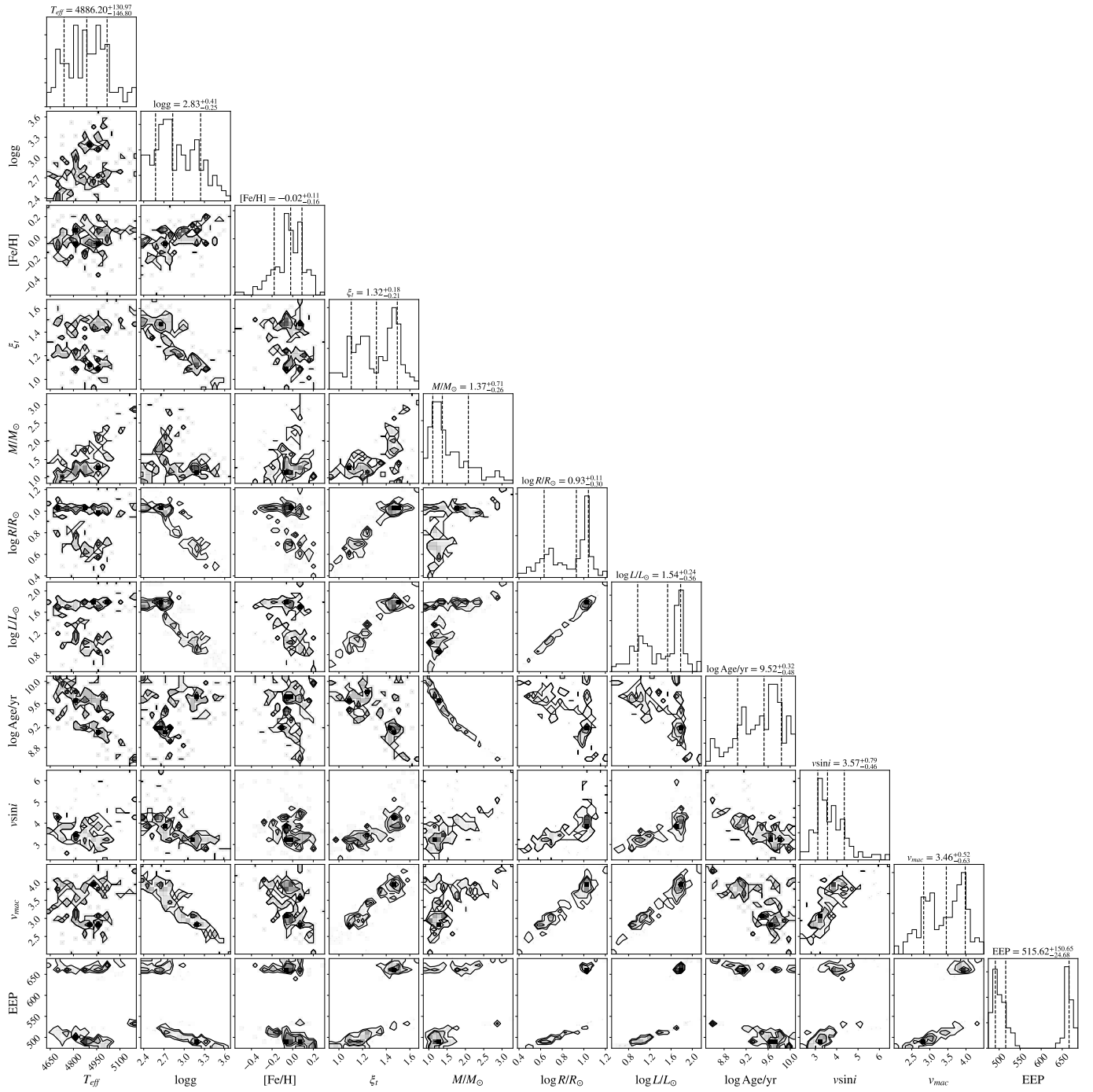


Fig. B.1. Correlations between all the parameters computed by SPECIES. Only a few of these are plotted in Figure 9.